

1996

Application of state-of-the-art FEM techniques to magnetostatic NDE

Gopichand Katragadda
Iowa State University

Follow this and additional works at: <https://lib.dr.iastate.edu/rtd>

 Part of the [Electrical and Electronics Commons](#), [Materials Science and Engineering Commons](#), [Mechanical Engineering Commons](#), and the [Petroleum Engineering Commons](#)

Recommended Citation

Katragadda, Gopichand, "Application of state-of-the-art FEM techniques to magnetostatic NDE " (1996). *Retrospective Theses and Dissertations*. 11116.
<https://lib.dr.iastate.edu/rtd/11116>

This Dissertation is brought to you for free and open access by the Iowa State University Capstones, Theses and Dissertations at Iowa State University Digital Repository. It has been accepted for inclusion in Retrospective Theses and Dissertations by an authorized administrator of Iowa State University Digital Repository. For more information, please contact digirep@iastate.edu.

INFORMATION TO USERS

This manuscript has been reproduced from the microfilm master. UMI films the text directly from the original or copy submitted. Thus, some thesis and dissertation copies are in typewriter face, while others may be from any type of computer printer.

The quality of this reproduction is dependent upon the quality of the copy submitted. Broken or indistinct print, colored or poor quality illustrations and photographs, print bleedthrough, substandard margins, and improper alignment can adversely affect reproduction.

In the unlikely event that the author did not send UMI a complete manuscript and there are missing pages, these will be noted. Also, if unauthorized copyright material had to be removed, a note will indicate the deletion.

Oversize materials (e.g., maps, drawings, charts) are reproduced by sectioning the original, beginning at the upper left-hand corner and continuing from left to right in equal sections with small overlaps. Each original is also photographed in one exposure and is included in reduced form at the back of the book.

Photographs included in the original manuscript have been reproduced xerographically in this copy. Higher quality 6" x 9" black and white photographic prints are available for any photographs or illustrations appearing in this copy for an additional charge. Contact UMI directly to order.

UMI

A Bell & Howell Information Company
300 North Zeeb Road, Ann Arbor MI 48106-1346 USA
313/761-4700 800/521-0600

Application of state-of-the-art FEM techniques to magnetostatic NDE

by

Gopichand Katragadda

A Dissertation Submitted to the
Graduate Faculty in Partial Fulfillment of the
Requirements for the Degree of
DOCTOR OF PHILOSOPHY

Department: Electrical and Computer Engineering
Major: Electrical Engineering (Electromagnetics)

Approved:

Signature was redacted for privacy.

In Charge of Major Work

Signature was redacted for privacy.

For the Major Department

Signature was redacted for privacy.

For the Graduate College

Members of the Committee:

Signature was redacted for privacy.

Iowa State University
Ames, Iowa
1996

UMI Number: 9620975

UMI Microform 9620975
Copyright 1996, by UMI Company. All rights reserved.

**This microform edition is protected against unauthorized
copying under Title 17, United States Code.**

UMI
300 North Zeeb Road
Ann Arbor, MI 48103

TABLE OF CONTENTS

ACKNOWLEDGMENTS	xi
CHAPTER 1. INTRODUCTION	1
Overview	1
Background	4
Historical Perspective	5
Analytical methods	6
Numerical methods	7
Current Trends in FEM	9
Scope of the Dissertation	10
CHAPTER 2. FLUX LEAKAGE TESTING APPLIED TO OPERATIONAL PIPELINES	12
Background	12
MFL Inspection of Pipelines	13
Anatomy of a Pig	14
Modeling Considerations	17
CHAPTER 3. AXISYMMETRIC FORMULATION FOR MAGNETOSTATIC PHENOMENA	21
Introduction	21

Governing Equation	22
The Weighted Residual Approach	23
Formulation of Axisymmetric Finite Element Galerkin Equations	24
Results and Analysis	26
CHAPTER 4. AXISYMMETRIC FORMULATION INCORPORATING VELOCITY	30
Introduction	30
Transient Analysis of Velocity Effects	31
The finite difference method of time stepping	32
The Leismann-Frind method for transient analysis	33
Results and Analysis	36
CHAPTER 5. NONLINEAR ANALYSIS INCORPORATING PERMEABILITY EFFECTS	45
Introduction	45
Iterative Solution of Nonlinear Equations	46
Application of the Nonlinear Formulation	47
Axisymmetric formulation	47
3D formulation	48
Results and analysis	48
CHAPTER 6. APPLICATIONS OF THE NONLINEAR AXISYMMETRIC CODE INCORPORATING VELOCITY	56
Introduction	56
Additional Modalities for Pipeline Inspection	57
Standard MFL	58

Variable reluctance	59
Motion induced RFEC	60
Motion induced currents at defect edges	61
CHAPTER 7. THREE-DIMENSIONAL MODELING OF VELOC-	
ITY EFFECTS	65
Introduction	65
A-V Formulation	66
Modified Vector Potential Formulation	67
Nodal Element Formulations	68
Divergence condition	68
Interface conditions	70
Corner singularities	70
Constructing nodal elements	72
Edge Element Formulations	73
Construction of edge elements	73
Properties of edge elements	74
Edge Element Based Mesh Generation	75
Formulation for the 3D Magnetostatic Motion-related Problem	77
The curl-curl term	77
The velocity term	79
The 3D governing equation	79
3D Galerkin finite element formulation	79
Jacobi transformation	81
Computational Aspects of 3D Edge Element Modeling	82

Memory considerations	82
Speed considerations	83
Results	84
CHAPTER 8. DATA-ACCESS METHODS FOR FINITE ELE-	
MENT DATA	89
Introduction	89
Data Description	90
Implementation Details	91
Components of a netCDF file	91
Creating and reading a netCDF file	93
Conclusions	94
CHAPTER 9. CONCLUSIONS	95
Summary of Accomplishments	95
Tool design	95
Analysis of the MFL signals	96
3D edge element code capable of modeling velocity effects	96
Future Directions	97
Optimizing the matrix solver	97
Incorporating nonlinearity into the 3D edge element code	98
Analyzing the 3D nature of velocity effects	98
BIBLIOGRAPHY	99

LIST OF TABLES

Table 7.1:	Shape functions for nodal elements	73
Table 7.2:	Shape functions for edge elements	75

LIST OF FIGURES

Figure 2.1:	The Vetco high-resolution pig	14
Figure 2.2:	Typical MFL inspection vehicle	15
Figure 2.3:	Magnetization of the pipe-wall	16
Figure 2.4:	Flux leakage at the defect	17
Figure 2.5:	BH curves used in the FEM code	19
Figure 2.6:	ID detection pig	20
Figure 2.7:	Cleaning pigs	20
Figure 3.1:	2D pig geometry (courtesy of Battelle, Columbus, Ohio) . . .	27
Figure 3.2:	Flux contours predicted by the axisymmetric code (the brush and pipe-wall regions are scaled to show detail)	27
Figure 3.3:	Radial and axial components of the flux density	28
Figure 3.4:	Variation of MFL signal for different defect lengths. Defect depths are 50 percent throughwall	29
Figure 3.5:	Variation of MFL signal for different defect depths. Defect widths are 0.09 m	29

Figure 4.1:	Velocity effects on the flux lines at 5 m/s, defect is 0.09 m long and 50 percent through wall (the brush and pipe-wall regions are scaled to show detail)	37
Figure 4.2:	Variation of MFL signal with velocity. Defects are 0.09 m long and 50 percent through wall	38
Figure 4.3:	Comparison of the values of the axial component of the flux density under the poles	39
Figure 4.4:	Comparison of the values of the radial component of the flux density under the poles	40
Figure 4.5:	Distribution of induced currents at defect edges. Defect is 0.09 m long and 50 percent through wall, and magnetizer velocity is 5 m/sec (scale indicates magnitudes in A/square-meter) . .	41
Figure 4.6:	Magnitude of induced currents under the defect. Defect is 0.09 m long and 50 percent through wall, and magnetizer velocity is 5 m/sec	42
Figure 4.7:	Velocity effects for a .05 m long, 50 percent through wall defect with the modified tool	42
Figure 4.8:	Comparison of transient and static analysis for a 0.09 m long 50 percent through wall defect	43
Figure 4.9:	Comparison of transient and static analysis for a 0.09 m long 80 percent through wall defect	43
Figure 4.10:	Comparison of transient and static analysis for a 0.05 m long 50 percent throughwall defect	44
Figure 5.1:	Operating points on the initial BH curve	47

Figure 5.2:	Comparison of experimental and FEM results with the magnetizer placed in air	49
Figure 5.3:	Comparisons of experimental and FEM results with the magnetizer place in a pipe	50
Figure 5.4:	Comparison of codes - axisymmetric defect and axisymmetric magnetizer	51
Figure 5.5:	MFL signal from axisymmetric defect with a 3D magnetizer .	52
Figure 5.6:	MFL signal from 3D defect with an axisymmetric magnetizer	53
Figure 5.7:	MFL signal from 3D defect with a 3D magnetizer	54
Figure 5.8:	Permeability distribution under an axisymmetric defect with an axisymmetric magnetizer	54
Figure 5.9:	Permeability distribution under a 3D defect with a 3D magnetizer	55
Figure 6.1:	Sensor positions associated with the additional modalities . .	58
Figure 6.2:	Typical MFL signals	59
Figure 6.3:	Typical VR signals	60
Figure 6.4:	Typical RFEC signals	62
Figure 6.5:	Currents at defect edges	63
Figure 6.6:	Skewing of the MFL signal due to induced currents at defect edges	64
Figure 6.7:	The effect of velocity of VR signal. Defect is 0.15 m long . .	64
Figure 7.1:	Difficulty of imposing interface conditions with nodal elements	71
Figure 7.2:	Hexahedral nodal element	72

Figure 7.3:	Hexahedral edge element	74
Figure 7.4:	Global numbering scheme	77
Figure 7.5:	Geometry and field lines corresponding to the MVP formulation (static case)	84
Figure 7.6:	Validation of the edge element code for the 2D static case . .	85
Figure 7.7:	The effect of velocity on the flux lines	86
Figure 7.8:	Comparison of edge element MVP formulation and nodal element MSP formulation	87
Figure 7.9:	Comparison of edge element MVP formulation and experiment	88
Figure 7.10:	Variation of an MFL signal with velocity - a 3D prediction .	88
Figure 8.1:	An example of a CDL file	92

ACKNOWLEDGMENTS

Dr. William Lord, my major advisor, has been a source of inspiration during my graduate program at ISU and will remain a major influence in the years to come. From him I have learnt both technical and inter-personal skills which will be the guiding beacons to my future. I am deeply indebted to Dr. Lord for his guidance and support. I thank him for all time he spent in helping make this work something I cherish.

This dissertation is largely an outcome of my daily interaction with Dr. Yushi Sun. From him I have acquired all my knowledge of Numerical Modeling. I am grateful to him for guiding me through the highs and lows of this study. I thank Dr. Lalita Udpa and Dr. Satish Udpa for their valuable input during our weekly group meetings. Their experience and knowledge have helped shape the goals of this project. I appreciate Dr. Glenn Leucke and Dr. Vinay Dayal for being on my committee and enriching this work with their suggestions.

I acknowledge with gratitude the help of my colleague, Jiatun Si, who generated the 3D MSP formulation results presented in this dissertation.

I cherish the support provided by my wife, Seema, and thank her for the help in proof-reading this dissertation. I dedicate this work to my first teachers - my parents.

Finally, I thank the Gas Research Institute for funding this work.

CHAPTER 1. INTRODUCTION

Overview

Historically, developments in the numerical modeling of electromagnetic phenomena followed closely on the heels of developments in the modeling of structural engineering and fluid dynamics problems. Modeling of electromagnetic phenomena, however, has its own peculiar problems and requirements. These include: 1) ensuring the divergence condition, 2) imposing material interface conditions, and 3) dealing with field singularities at conductor corners. Recent development of new modeling algorithms better suited for electromagnetic applications, and the availability of low-cost/high-speed digital computers, call for a re-evaluation of the numerical methods currently being used for electromagnetic modeling. An industrial problem which is a typical example of the complexities involved in modeling electromagnetic phenomena, is that of modeling the magnetic flux leakage inspection of gas transmission pipelines. The problem calls for the three-dimensional (3D) modeling of motionally induced currents (using transient analysis), modeling the nonlinearity of the ferromagnetic parts, and the accurate modeling of the permanent magnet used in the magnetizer. To quote a leading authority on this topic: "Formidable complications arise, [however], when solution methods are considered. These are due to the non-linear, hysteretic behavior of line-pipe steel, to the changing geometry resulting from

the relative motion between the defect and detector, and the need to consider 3D modeling for realistic defects. The result is that there is very little hope of obtaining analytic solutions without seriously oversimplifying the problem. The prospects for numerical solutions using, for example, modern finite element calculation techniques are not much better. The detailed computation of such three-dimensional, nonlinear, transient effects is somewhat beyond the capabilities of both current state-of-the-art computer hardware and software” [1]. Researchers, have thus far simplified the problem using several assumptions, including that of axisymmetry, and modeling velocity effects using steady-state analysis. However, there has been no attempt to quantify the errors introduced by these assumptions. Also, due to the unavailability of commercial codes to solve 3D motion-related problems using transient analysis, a detailed study of the true nature of velocity effects has not been possible.

This dissertation implements and evaluates state-of-the-art finite element modeling techniques applied to the specific problem of modeling magnetic flux leakage inspection of gas pipelines. This provides the basis to draw conclusions on the general problem of modeling magnetostatic phenomena. The problem is approached from the simplest perspective, gradually building on the complexity of the model as both experimental and model results indicate the need for improvement. Initially, an axisymmetric finite element formulation is utilized to model the magnetic flux leakage inspection of gas pipelines. The need to model velocity effects is demonstrated using simulated leakage field signals with and without velocity effects. Also, the need for transient analysis, as opposed to steady-state analysis, is argued using a comparison of results for each case. The origin and nature of velocity effects is researched as part of this study. The nonlinearity of permeability for ferromagnetic parts of the

geometry is discussed. Experimentally obtained BH curves are used to incorporate nonlinearities in different portions of the geometry being studied. Results are presented showing the usefulness of the axisymmetric model in providing a qualitative understanding of the physical phenomena involved. The results include: 1) finite element predictions demonstrating the presence of alternative modalities initiated by the magnetic flux leakage tool, which contain valuable defect information, and 2) examples of tool-design ideas provided by a detailed study of the predicted field distributions.

Defects encountered in pipeline inspections are rarely axisymmetric. The magnetizer used, is also, most often not truly axisymmetric. This necessitates 3D modeling of the geometry. A study is conducted showing the differences between axisymmetric approximations and full 3D predictions. As part of this study, the finite element code is experimentally validated. Serious problems (including spurious solutions and corner singularities) associated with the traditional node-based finite-element techniques, when applied to the 3D modeling, are discussed. New and efficient numerical modeling concepts, using the edge-based finite-element technique, are proposed to overcome these problems. A 3D edge element code is developed and tested for modeling magnetic flux leakage, incorporating velocity effects.

There are several aspects to finite element modeling including: choice of variables, choice of element, mesh generation, choice of matrix solver and data storage formats. Each of these aspects is discussed in this dissertation. The state-of-the art in numerical modeling of motion related magnetostatic phenomena, prior to this work, was limited to the steady state analysis of 3D problems using nodal elements. This dissertation advances the capability to a transient analysis of 3D problems, using

edge elements.

Background

Maxwell's equations, conceived 120 years ago, provide the starting point for any discussion dealing with the numerical modeling of electromagnetic phenomena. Maxwell formalized the theory of electromagnetism in mathematical terms. The equations which go under his name can be written in both differential and integral forms. The differential form leads to the differential equations used in finite element modeling (FEM). For magnetostatic phenomena, which is the nature of the problem discussed in this work, Maxwell's equations in the differential form can be written as

Faraday's law:

$$\nabla \times \mathbf{E} = 0 \quad (1.1)$$

Maxwell-Ampere law:

$$\nabla \times \mathbf{H} = \mathbf{J} \quad (1.2)$$

Gauss' law:

$$\nabla \cdot \mathbf{D} = \rho \quad (1.3)$$

Gauss' law - magnetic:

$$\nabla \cdot \mathbf{B} = 0 \quad (1.4)$$

Another fundamental equation, which is known as the equation of continuity, can be written (for the magnetostatic case) as:

$$\nabla \cdot \mathbf{J} = 0 \quad (1.5)$$

Only three of (1.1) - (1.5) are independent equations. Either (1.1), (1.2) and (1.3) or (1.1), (1.2) and (1.5) can be chosen as such independent equations. The other two equations in each case can be derived from the respective independent equations.

By formalizing electromagnetic fields in mathematical terms, Maxwell provided a basis for utilizing mathematical tools to understand electromagnetic phenomena. During the past 120 years several innovative methods, discussed in the following section, have been developed for solving electromagnetic problems. However, the solutions of Maxwell's equations for practical situations had to await recent advances in computer hardware and numerical algorithms. Only in recent years has it become possible for an engineer to investigate the electromagnetic nature of complex devices using field theory. Three developments are responsible for making this possible: 1) availability of reasonably priced high speed computers for the data-intensive modeling, 2) availability of graphics computers for visualization of field geometries and field distributions, and 3) advances in numerical techniques which represent geometries and Maxwell's equations in a digital or discrete form.

Historical Perspective

The method of solution of the partial differential equations (PDEs) associated with electromagnetic field problems could be analytical or numerical. In analytical methods, the solution takes the form of an algebraic function into which the values of parameters defining the particular problem can be substituted. Generally, analytical methods are possible only for simple cases where the fields are or can be treated as two-dimensional, the properties of the media occupying the field are linear and the time variation is relatively simple. Numerical methods, take the form of a particular

set of numerical values of the function describing the field for one particular set of values of physical parameters. Numerical methods are more versatile and can be applied to a wide range of problems. Analytical methods have provided the classical approach for at least 90 years, but in the last 30 years, numerical methods have been developed in very powerful forms and are most often the methods of choice.

Analytical methods

Several analytical approaches are available for solving electromagnetic problems. Important amongst them are: the image method, separation of variables and conformal transformations.

The method of images can be used to give particularly elegant solutions to some important problems involving straight-line or circular boundaries. The method offers ready-made solutions which eliminate the need for formal solutions of Laplace's and Poisson's equations. The idea of images is due to Lord Kelvin, but Maxwell, Lodge [2] and Searle [3] extended this approach.

Perhaps the most powerful analytical method is the separation of variables. This method entails breaking up the PDE into a product of functions, each of which involves only one variable. This method is applicable only if the functions being solved are completely separable.

Conformal mapping is the representation of a bounded area in the plane of a complex variable by an area in the plane of another complex area. Thus this method is a branch of mathematics based on the theory of functions of a complex variable. J.J. Thompson introduced conformal mapping to electromagnetics in his book *Recent Researches in Electricity and Magnetism* (1893) [4]. F.W. Carter was the first to apply

conformal mapping to an actual engineering problem [5]. Conformal mapping has proven to be a particularly powerful method for the solution of Laplacian fields with complicated boundary shapes.

Numerical methods

Analytical methods are available only for the simplest of geometries. It is rare for electromagnetic problems to fall neatly into a class that can be solved by analytical methods [6]. Solving electromagnetic nondestructive evaluation (NDE) problems, which involve considering complicated defect shapes and geometries, necessitate the use of numerical modeling. Initial attempts by engineers to model electromagnetic devices were based on lumped parameter circuit models [7]. Circuit theory is derived from field theory under certain assumptions and large simplifications, and hence can provide only a qualitative understanding of the electromagnetic phenomena being modeled. However, transmission-line modeling (TLM), a method similar to the lumped circuit model, has proven to be a powerful modeling technique. TLM is a numerical technique for solving field problems based on the equivalence between Maxwell's equations and the equations for voltages and currents on a mesh of continuous two-wire transmission lines [8]. The main feature of this method is the simplicity of formulation and programming for a wide range of applications. As compared with the lumped network model, the transmission line model is more general and performs better at high frequencies where the transmission and reflection properties of geometrical discontinuities cannot be regarded as lumped. The TLM method is limited only by the amount of memory storage required, which depends on the complexity of the TLM mesh [9].

Advances in computer technology, have allowed numerical solutions to problems in terms of field theory. Important amongst this class of solution methods are the finite difference modeling (FDM) and the finite element modeling (FEM) techniques. FDM was the first numerical method used to solve Maxwell's equations in their differential form. FDM is based upon approximations which permit replacing differential equations by finite difference equations. FDM was first developed by A.Thom [10] in the 1920's under the title "the method of squares" to solve nonlinear hydrodynamic equations. Since then, the method has found applications in solving a variety of field problems. On the other hand, FEM has its origin in the field of structural analysis. Courant's paper in 1943 dealing with elasticity problems can be considered as the earliest work with FEM. However, the method was not applied to electromagnetic problems until 1968. Winslow's work [11] in applying FEM to electromagnetics is amongst the first significant publications in this area. Although FDM and TLM are conceptually simpler and easier to program than FEM, FEM is a more powerful and versatile numerical technique for handling problems involving complex geometries and inhomogeneous media. Hence FEM is the most popularly used numerical method in solving NDE problems [12].

There are several other numerical methods which have not been included in this discussion, including the method of moments (MOM) and the Monte-Carlo method. Also, the scope of this discussion has been limited to the domain methods for solving Maxwell's equation in their differential form. For this reason the whole branch of integral methods applied to computational electromagnetics has not been included in this section. An excellent introduction to these and other numerical techniques applied to electromagnetics is available in [9].

Current Trends in FEM

Classical FEM methods use nodal elements, with scalar shape functions, to approximate electromagnetic field quantities. These methods extend to vector fields, methods which were originally developed for scalar fields. In these methods, the vector field is considered as a triplet of scalar fields in some coordinate system. This technique has proved to be extremely useful in the past, especially in 2D modeling. However, serious problems are observed when this technique is employed in the 3D modeling of vector fields. First, is the problem of spurious solutions, which are generally attributed to not satisfying the divergence condition. Second, is the difficulty of imposing boundary conditions at material interfaces. Third, is the problem of field singularities at corners of conducting materials.

The edge element method is a revolutionary approach which has recently gained extreme importance in the modeling of vector fields. This method uses elements with degrees of freedom attached to edges rather than nodes. These elements have vectorial shape functions, and hence are better suited for modeling vector field problems. The vector finite elements of which edge elements form a sub-class were described in 1951 by Whitney [13]. However, their use in electromagnetics was not realized until recently. In 1980, Nedelec discussed tetrahedral and rectangular brick edge elements [14]. Bossavit and Verite applied tetrahedral edge elements to 3D eddy-current problems [15]. Hano, in an independent attempt, introduced rectangular edge elements for the analysis of dielectric waveguides [16]. Mur and de Hoop considered the problem of electromagnetic fields in inhomogeneous media [17]. Van Welij [18] and Kameari [19] further developed the application of edge elements to eddy current modeling. More recently, Barton and Cendes employed tetrahedral edge elements for

3D magnetic field computations [20]. In all of these works edge elements have been shown to be free of all the previously mentioned shortcomings associated with nodal elements.

Scope of the Dissertation

The underlying theme of this dissertation is the magnetic flux leakage (MFL) inspection of gas pipelines. The focus is on the accurate numerical modeling of the associated phenomena. Chapter 2 introduces the technical aspects of MFL inspection of gas pipelines. The geometry of the magnetizer is described in detail, with special focus on the characteristics of the permanent magnet and the nonlinear characteristics of the ferromagnetic parts. This chapter discusses the variabilities which need to be included in the numerical model.

The governing equation for the axisymmetric formulation of a magnetostatic problem is briefly described in Chapter 3. Typical results from the FEM code are explained. The results are used to present an understanding of the basic principles of MFL inspection.

Chapter 4 reviews, in brief, the different methods available to incorporate velocity effects into the numerical model. Results showing the need for incorporating velocity effects are presented. Also, the need for transient analysis is demonstrated by comparing steady-state and transient solutions. The role of the time derivative term in the governing equation for electromagnetic problems dealing with motion is analyzed.

The nonlinearity characteristics of the ferromagnetic parts (pipe-wall and magnetizer) are discussed in detail in Chapter 5. Special attention is drawn to the

saturation of the pipe-wall in the vicinity of defects. The method of incorporating nonlinearities is explained and the corresponding results presented. Results showing the differences in pipe-wall saturation for the 3D and axisymmetric cases are included. The experimental validation of the FEM code is part of this discussion.

Chapter 6 presents applications of the axisymmetric code incorporating nonlinearity and velocity effects. The code is exercised to study the availability of untapped NDE modalities inherent in the MFL tool, showing the usefulness of the model in understanding the physics of energy-defect interaction.

Chapter 7 introduces 3D modeling concepts. A detailed discussion is provided, on the advantages of the edge element method which is currently gaining popularity for modeling vector fields. Special attention is paid to the reasoning for the necessity of the edge element technique, to model accurately the MFL inspection tool, in 3D, incorporating velocity effects. Theoretical background and implementation details are provided. Results from a 3D edge element code, applied to modeling the MFL inspection situation including velocity effects, are included.

Chapter 8 is a study of the data storage problem for the numerical model output. The need for an efficient, self describing, network transparent, data storage scheme is discussed. The implementation of a data storage scheme using eXternal Data storage (XDR) with netCDF (a free public domain software) is detailed.

The conclusions of this study and future directions are presented in Chapter 9.

CHAPTER 2. FLUX LEAKAGE TESTING APPLIED TO OPERATIONAL PIPELINES

Background

It is estimated that there are about one million kilometers of gas and liquid transmission pipelines operating across the globe today. Pipelines, owing to their strategic role of transporting gas and liquid fuels, are of immense capital value. Potential degradation and failure of pipelines is a sensitive issue both with the public and legislative bodies, since the consequences of failure could include injuries and death. In addition, pipeline failures have severe financial consequences. More than half the pipelines in use today are 30 or more years old and invariably have experienced some deterioration. Preventive maintenance using NDE techniques plays an important role in ensuring safe pipeline operation [21].

When viewed as an application for NDE, pipelines present immediate difficulties for online inspection. Since the only practical approach to a detailed inspection of the pipeline is from the inside, the method used must overcome problems posed by the pipeline geometry and the pipeline product. The product is usually pressurized, and could be extremely hot or chemically aggressive. The inspection method must be fast and hence stable under the dynamic conditions. The method selected for the inspection also depends on the defect-class of particular interest. Conditions such

as fatigue, stress corrosion and laminations result in cracking of the pipeline. The ultrasonic method has proven to be the optimal method for detecting these conditions. Gouging, spalling and corrosion result in metal-loss defects. MFL inspection, has, over the years proven to be the most effective technique in achieving the required performance for metal-loss inspection in a pipeline environment [22].

MFL Inspection of Pipelines

Conventional MFL inspection vehicles are termed pigs. Figure 2.1 shows a pig termed the high-resolution pig, designed and built by Vetco Pipeline Services. Figure 2.2 shows a schematic of the cross-section of a typical pig. Since the mid-1960's, the pipeline industry has utilized such instrumented pigging systems to conduct in-line inspection of pipelines to detect various piping defects [23]. Intensive research has gone into the efficient design and development of pigs. The pig in Figure 2.1 is the end product of several years of innovative technology being applied to: 1) the mechanical design - enabling the pig to move through the pipelines negotiating bends and girth welds, propelled by the pressure of the gas, 2) the hardware design - miniaturization of which has made possible placing the data-acquisition system in a pressurized chamber on board the pig, and 3) the magnetic circuit design - improvements in which have made possible inspection of even thick walled pipelines, which was previously a bottleneck in MFL inspection.

The pig magnetizes the ferromagnetic pipe-wall in between the two brushes (Figure 2.3). The presence of a defect in the pipe-wall results in a redistribution of magnetic field in the vicinity of the flaw, causing some of the magnetic field to leak out (Figure 2.4). The leakage field is detected using Hall element sensors to measure the

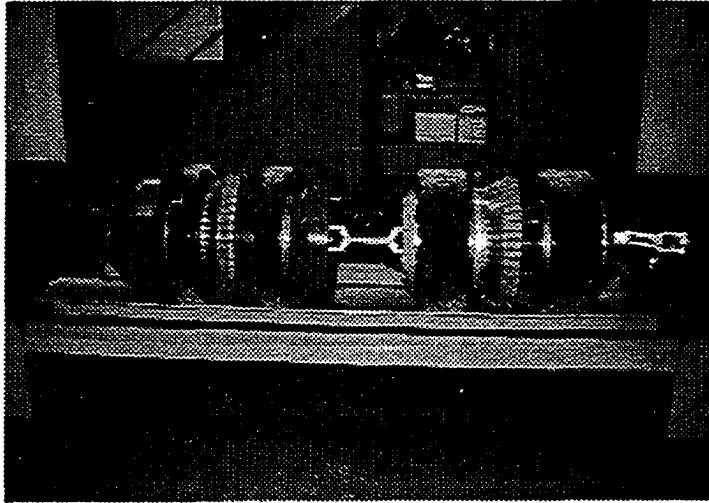


Figure 2.1: The Vetco high-resolution pig

axial or radial components of the magnetic flux density \mathbf{B} . This constitutes active leakage field measurement, which is well documented in the literature [24].

Anatomy of a Pig

Many different designs pig designs are used in the industry, though with the same working principle. Pigs are available for pipelines varying in diameter from 0.1m-1.2m. The geometry of the high-resolution pig is described in this section, to provide insight into the design of a pig. The high-resolution pig used by Vetco Pipeline Services consists of two units connected by a universal joint. The universal joint allows flexibility of the unit enabling it to negotiate bends in pipelines. The front unit is used to flag defects as either inner-diameter (ID) or outer-diameter (OD). It has ninety six circumferentially distributed magnet-detector coil assemblies which provide the ID/OD flag using the variable reluctance principle. The steel brushes

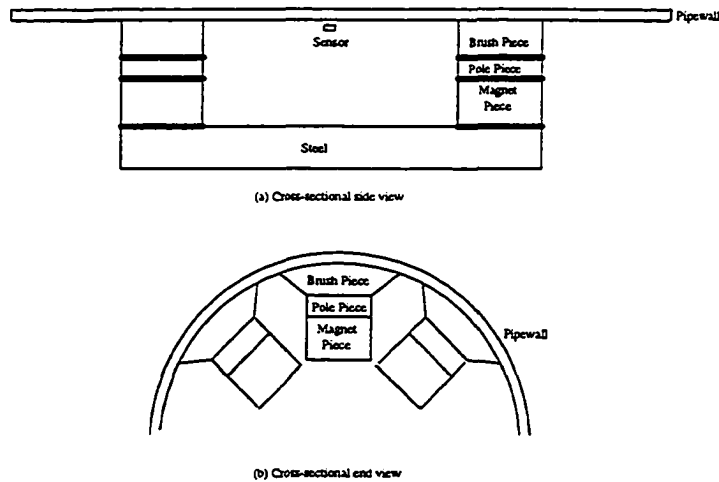


Figure 2.2: Typical MFL inspection vehicle

on the front unit provide mechanical support for the pig. The rear unit houses the actual MFL tool and is described next.

The magnetic circuit of the MFL tool consists of the magnet assembly, the backing iron and the brushes. The magnet assembly consists of several (approximately .01m width, .01m height, .04m length) neodymium magnets, with curved surface and beveled edges, glued circumferentially in a close fit. This arrangement provides an axisymmetric field. Neodymium magnets have ten times the strength, measured in energy per unit volume, of Alcomax magnets used in early pigs. This is the major factor enabling the pig to inspect thick walled pipes. The backing iron is an important part of the magnetic circuit and improper design would cause most of the magnetomotive force to drop across the backing iron rather than in the pipe-wall. The cross-sectional area of the backing iron is typically 1.25 times the pipe-wall cross-sectional area. The length of the backing iron between the two poles can be varied. It has been noticed that the greater the length of the backing-iron, the smaller the

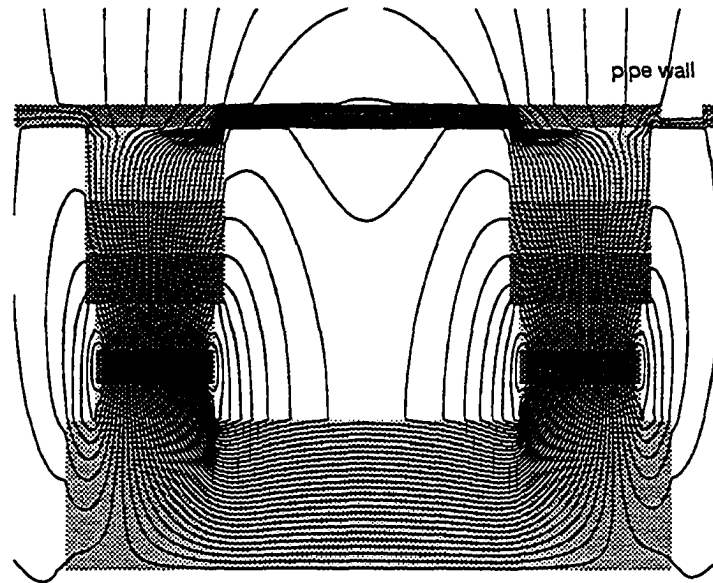


Figure 2.3: Magnetization of the pipe-wall

velocity effects on the MFL signal. The brushes are made of steel bristles. They provide mechanical support in addition to providing a flexible contact with the pipe-wall for the magnetic circuit. The brush region is the most difficult to model numerically, since the characteristics of the brushes are not easy to measure. Generally, only 15% of the brush area is considered to be metal. Typically, the cross-sectional area of the brush is 3-5 times the pipe-wall cross-sectional area.

In addition to the magnetic circuit, other important parts of the pig are: the Hall element sensors, the odometer and the data acquisition system. Ninety six circumferentially distributed Hall element sensors measure the axial component of the flux density \mathbf{B} using the Hall-effect principle. The odometer provides information regarding the location of the defect, the velocity of the pig in various sections of the pipe and also triggers the data acquisition for incremental motion of the pig. The data

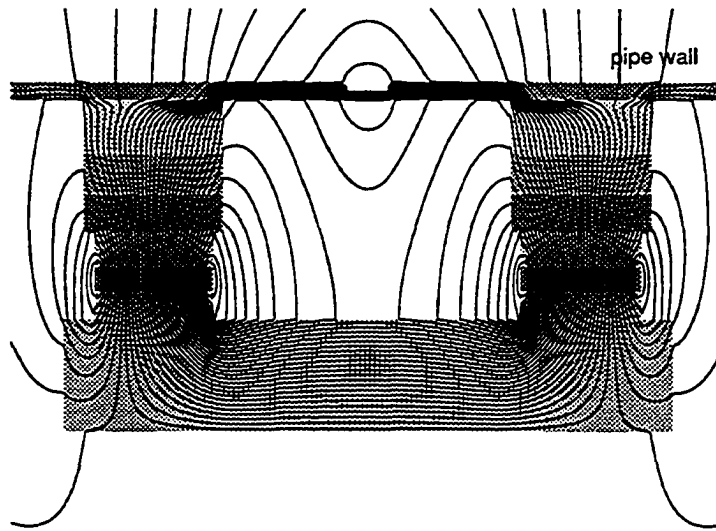


Figure 2.4: Flux leakage at the defect

acquisition system is placed in a pressurized chamber. This system is 486 processor based, and is capable of storing the data generated (typically 3-4 mega bytes) in a single run of the pig, on a hard disk mounted on board. The parts of the pig in contact with the pipe-wall (other than the brushes) are made of flexible plastic material. The diameter of these parts is slightly larger than the pipe diameter to provide a mechanically stable air-tight fit for the pig. This allows the pig to be propelled under the pressure of the gas.

Modeling Considerations

In modeling the geometry shown in Figure 2.2 several variables have to be accurately specified including, 1) the dimensions of the different parts, 2) the coercivity of the permanent magnet, and 3) the nonlinear BH curves for the ferromagnetic parts. Whereas the dimensions of the geometry can be accurately controlled by the

manufacturer, it is more difficult to control, exactly, the nonlinear behavior of the ferromagnetic parts or the coercivity of the magnet.

Since the permanent magnet is the source of the magnetic field for the MFL inspection, the ability to predict quantitatively accurate results depends largely on the accuracy of the coercivity of the magnet used in the model. Since the manufacturer specified coercivity did not result in the desired accuracy from the FEM codes, experiments were conducted at the Battelle Memorial Research Center, Columbus, Ohio, to estimate the coercivity. While the manufacturer specified coercivity was 8.58×10^5 A/m, experiments estimated the coercivity at 6.02×10^5 A/m. By varying the coercivity in the FEM code in this range, it was found that a coercivity of 7.65×10^5 A/m gave the best match between FEM predictions and experiments conducted as described in Chapter 6.

The pipe-wall in gas pipelines is specified to be grade X52. The backing-iron of the magnetizer is made of mild steel (0.18 % C). BH curves used for the pipe-wall and the backing-iron are shown in Figure 2.5. These curves have been obtained after modifying the manufacturer specified curves, such that an optimal match between FEM predictions and experimental results could be obtained.

The gas pipeline industry uses several other pigs to serve a variety of purposes. Figure 2.6 shows the pig used by Vetco pipeline services to measure ID changes, using spring loaded flaps. These detect defects such as dents or simply indicate pipe diameter / wall thickness changes. Figure 2.7 shows pigs used for cleaning the pipeline of debris. These pigs, which are built of carbide coated foam, are launched into the pipeline prior to sending in the MFL inspection pig.

More details on pigs and their use in pipeline inspection can be found in refer-

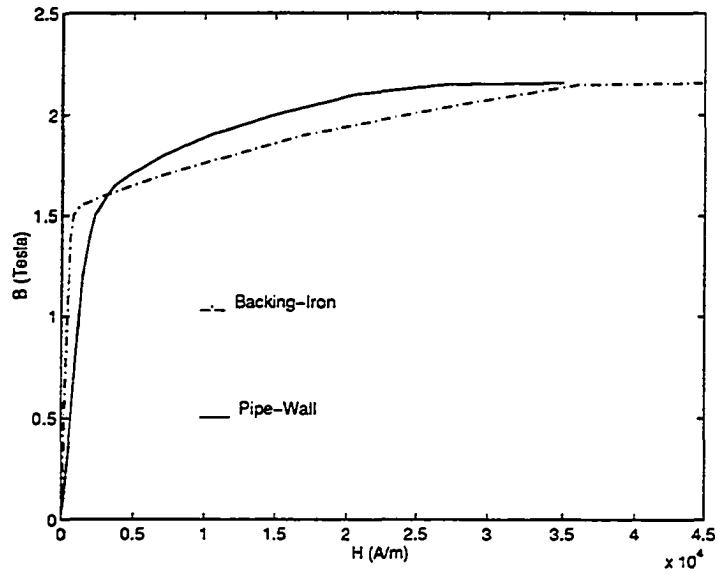


Figure 2.5: BH curves used in the FEM code

ences [22] and [25] to [29]

This chapter provides the background for the following chapters, which discuss the numerical modeling techniques that enable the simulation of signals generated by actual pigs. The next chapter discusses the first approximation in modeling the pig, ignoring velocity and permeability effects and assuming axisymmetry. The results from this model are used to explain how MFL signals are used to characterize defects.

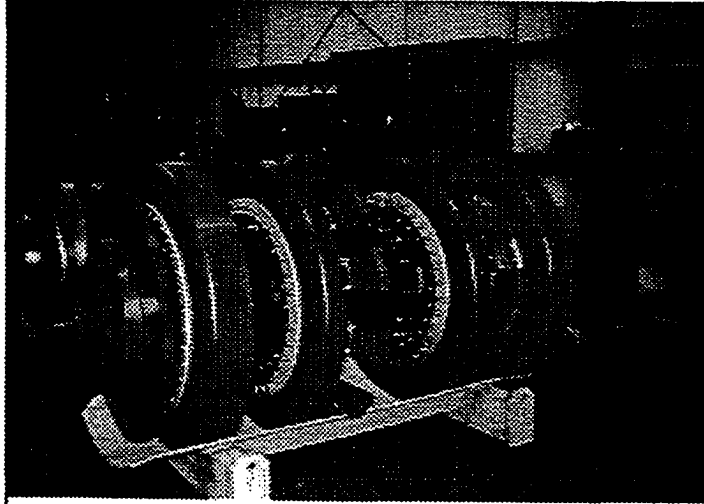


Figure 2.6: ID detection pig

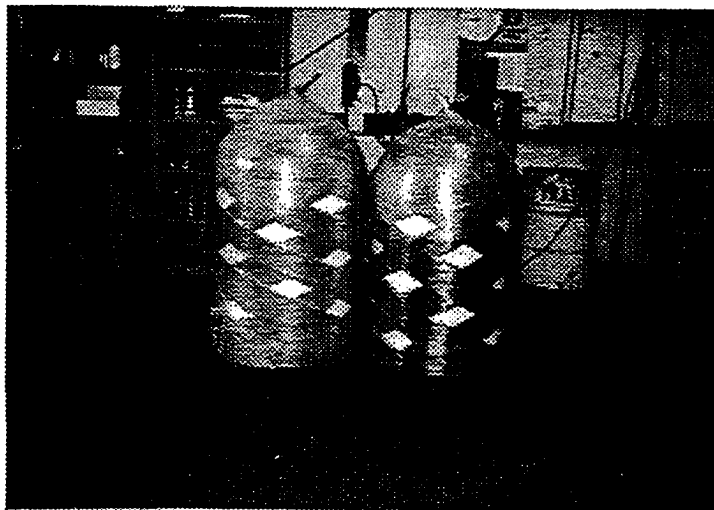


Figure 2.7: Cleaning pigs

CHAPTER 3. AXISYMMETRIC FORMULATION FOR MAGNETOSTATIC PHENOMENA

Introduction

The governing equation solved using FEM depends on the choice of the variable. FEM of magnetostatic fields, in terms of field quantities (\mathbf{E} , \mathbf{H} , \mathbf{B} , \mathbf{D} or \mathbf{J}), would be ideal since they are the quantities of interest. However they are all discontinuous over boundaries and material interfaces: $D_{1t} \neq D_{2t}$, $E_{1n} \neq E_{2n}$ when $\epsilon_1 \neq \epsilon_2$; $B_{1t} \neq B_{2t}$, $H_{1n} \neq H_{2n}$ when $\mu_1 \neq \mu_2$; $J_{1t} \neq J_{2t}$ when $\sigma_1 \neq \sigma_2$ (where t and n denote the tangential and normal components). These discontinuities are difficult to model in a traditional node-based finite element simulation. Hence auxiliary variables such as the magnetic scalar potential (ψ) and the magnetic vector potential (\mathbf{A}) have been traditionally used in solving magnetostatic problems using finite element techniques. The magnetic scalar potential formulations can be used only in the case where there are no currents in the solution region. Since magnetostatic problems involving motion include motionally generated currents in the solution region, this dissertation discusses only magnetic vector potential (MVP) formulations. This chapter looks at the MVP formulation for the case where motional terms can be neglected or are absent. A linear, axisymmetric, finite element implementation of the solution is discussed. Results are presented showing the axial and radial components

of the magnetic flux density \mathbf{B} . The principle of defect characterization using MFL is explained based on these results. This chapter provides the background for the following chapters where velocity effects, nonlinearity and 3D modeling are described.

Governing Equation

As discussed above, the auxiliary variable \mathbf{A} is used as a convenience in solving field problems using FEM. The MVP formulation follows from the definition of \mathbf{A} : since $\nabla \cdot \mathbf{B} = 0$ (Gauss' law - magnetic), we can define \mathbf{A} such that $\nabla \times \mathbf{A} = \mathbf{B}$. Using $\nabla \times \mathbf{H} = \mathbf{J}_s$ (Maxwell-Ampere's law), we can arrive at the governing elliptic partial differential equation:

$$\nabla \times \frac{1}{\mu} \nabla \times \mathbf{A} = \mathbf{J}_s \quad (3.1)$$

In axisymmetric and 2D cases there is only one component of \mathbf{A} , hence Coulombs gauge ($\nabla \cdot \mathbf{A} = 0$) is automatically satisfied. Using the vector identity: $\nabla \times \nabla \times \mathbf{A} = \nabla(\nabla \cdot \mathbf{A}) - \nabla^2 \mathbf{A}$, and assuming linearity and Coulombs gauge, we can write the governing equation as:

$$\frac{1}{\mu} \nabla^2 \mathbf{A} = -\mathbf{J}_s \quad (3.2)$$

here, ∇^2 is used to indicate the vector Laplacian operation. For the axisymmetric case Equation 3.2 reduces to:

$$\frac{1}{\mu} \left[\frac{\partial^2 \mathbf{A}}{\partial r^2} + \frac{1}{r} \frac{\partial \mathbf{A}}{\partial r} + \frac{\partial^2 \mathbf{A}}{\partial z^2} + \frac{\mathbf{A}}{r^2} \right] = -\mathbf{J}_s \quad (3.3)$$

Here, \mathbf{A} is assumed to have a component in the ϕ direction only. A finite element approach to the solution of Equation 3.3 is discussed in the next section.

The Weighted Residual Approach

Two methods of approximations form the basis of modern FEM. One is the variational approach, of which the Ritz variational approximation is the most popular. The second is the weighted residual method, of which the Galerkin's method is found to be the most accurate. In the variational approach, the problem is formulated in terms of a variational expression, referred to as a functional, whose minimum corresponds to the governing differential equation under the given boundary conditions. The approximate solution is then obtained by minimizing the functional with respect to its variables. There are several advantages to variational methods. The primary advantage is its well established solid foundation in physics and mathematics, which may permit a physical interpretation of the problem. Another advantage is that through the variational procedure one can clearly demonstrate the differences between the essential and natural boundary conditions [30]. Other advantages include the convenience of description and elegance of formulation. Due to these advantages, variational methods were generally preferred over Galerkin's method, in the past. The disadvantage with the variational method, particularly in electromagnetics, is that the method does not start directly from the differential equation, but rather starts from a variational formulation. Therefore the applicability of the method depends on the availability of such a formulation. The weighted residual method, described in this section, starts directly from the differential equation and hence is the preferred method for general electromagnetic problems.

A general representation of a boundary value problem (to which class equation 3.3 belongs), in a domain Ω is:

$$\mathcal{L}\phi = f \quad (3.4)$$

together with the boundary conditions on the boundary Γ that encloses the domain. In Equation 3.4, \mathcal{L} is a differential operator, f is the excitation or forcing function, and ϕ is the unknown quantity. Assume that $\tilde{\phi}$ is an approximate solution to Equation 3.4. Substitution of $\tilde{\phi}$ for ϕ would then result in a nonzero residual:

$$r = \mathcal{L}\tilde{\phi} - f \neq 0 \quad (3.5)$$

The best approximation for $\tilde{\phi}$ will be the one that reduces the residual r to the least value on all points of Ω . The weighted residual method enforces the condition:

$$\mathcal{R}_i = \int_{\Omega} w_i r d\Omega = 0 \quad (3.6)$$

where \mathcal{R}_i denotes the weighted residual integral and w_i is a chosen weighting function. In Galerkin's method, the weighting function is chosen to be the same as the shape functions used in the finite element solution. The application of Galerkin's method to Equation 3.3 is now explained.

Formulation of Axisymmetric Finite Element Galerkin Equations

The Galerkin weighted residual technique is now applied to Equation 3.3 to yield the finite element equations. The weighted form of the governing equation (equation 3.3) is:

$$\int_s w_j \left[\frac{1}{\mu} \left(\frac{\partial^2 \mathbf{A}}{\partial r^2} + \frac{1}{r} \frac{\partial \mathbf{A}}{\partial r} + \frac{\partial^2 \mathbf{A}}{\partial z^2} - \frac{\mathbf{A}}{r^2} \right) + \mathbf{J}_s \right] ds = 0 \quad (3.7)$$

Using the nodal element approximation:

$$\mathbf{A} = \sum_k \mathbf{A}_k N_k \quad (3.8)$$

and integrating by parts, Equation 3.7 is rewritten as (for node j):

$$\begin{aligned} & \sum_{i=1}^k \int_s \left(\frac{1}{\mu} \frac{\partial w_j}{\partial r} \frac{\partial N_i}{\partial r} \mathbf{A}_i \right) ds - \oint_c \left(w_j \frac{\partial \mathbf{A}_i}{\partial r} \right) dc \\ & + \int_s \left(\frac{1}{\mu r} w_j \frac{\partial N_i}{\partial r} \mathbf{A}_i \right) ds + \int_s \left(\frac{1}{\mu r} \frac{\partial w_j}{\partial r} N_i \mathbf{A}_i \right) ds \\ & \quad \int_s \left(\frac{1}{\mu} \frac{\partial w_j}{\partial z} \frac{\partial N_i}{\partial z} \mathbf{A}_i \right) ds - \oint_c \left(w_j \frac{\partial \mathbf{A}_i}{\partial z} \right) dc \\ & - \int_s \left(\frac{1}{\mu r^2} w_j N_i \mathbf{A}_i \right) ds + \int_s (w_j \mathbf{J}_s) ds = 0 \end{aligned} \quad (3.9)$$

where s is the two dimensional surface of the element and c is the contour enclosing the surface.

In the Galerkin method the shape functions are chosen as the weighting functions. Hence Equation 3.9 can be written as:

$$\begin{aligned} & \sum_{i=1}^k \int_s \left(\frac{1}{\mu} \frac{\partial N_j}{\partial r} \frac{\partial N_i}{\partial r} \mathbf{A}_i \right) ds - \oint_c \left(N_j \frac{\partial \mathbf{A}_i}{\partial r} \right) dc \\ & + \int_s \left(\frac{1}{\mu r} N_j \frac{\partial N_i}{\partial r} \mathbf{A}_i \right) ds + \int_s \left(\frac{1}{\mu r} N_i \frac{\partial N_j}{\partial r} \mathbf{A}_i \right) ds \\ & \quad + \int_s \left(\frac{1}{\mu} \frac{\partial N_j}{\partial z} \frac{\partial N_i}{\partial z} \mathbf{A}_i \right) ds - \oint_c \left(N_j \frac{\partial \mathbf{A}_i}{\partial z} \right) dc \\ & - \int_s \left(\frac{1}{\mu r^2} N_j N_i \mathbf{A}_i \right) ds + \int_s (N_j \mathbf{J}_s) ds = 0 \end{aligned} \quad (3.10)$$

The procedure is carried out over all the nodes.

The line integral terms in Equation 3.10 are important in the application of the finite element technique. The homogeneous Neumann condition is automatically but weakly satisfied at a boundary between two elements by setting these terms equal to zero. The Dirichlet boundary condition on the other hand is satisfied by imposing the fixed values on the matrix.

Results and Analysis

The axisymmetric formulation is now applied to simulate the MFL inspection technique corresponding to the geometry of Figure 3.1. A contour plot of the fields produced by the magnetizer is shown in Figure 3.2. The contour plot demonstrates clearly the principle of MFL inspection. The flux produced by the magnetizer is disrupted by the presence of the defect in the pipe-wall, causing some of the field to leak out of the material in the vicinity of the defect. The radial (\mathbf{B}_r) and axial (\mathbf{B}_z) components of the flux density, predicted by the FEM code are shown in Figure 3.3. These measurements correspond to the signal picked up by a hall element sensor placed just below the pipe-wall, exactly in-between the two brushes, as the magnetizer moves from the left to the right in Figure 3.2. Since the axial component of the flux density is, currently, the signal being used by the pipeline inspection industry for defect indications, we limit the discussion in this chapter to the \mathbf{B}_z component.

Figure 3.4 shows the variation of \mathbf{B}_z for different defect lengths and Figure 3.5 shows the variation of \mathbf{B}_z for different defect depths. For purposes of this dissertation, defect length refers to the axial extent of the defect in meters, defect depth refers to the percentage depth in terms of the wall thickness, and defect width refers to the

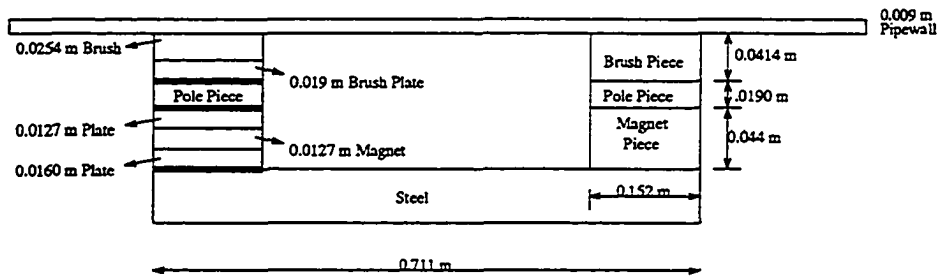


Figure 3.1: 2D pig geometry (courtesy of Battelle, Columbus, Ohio)

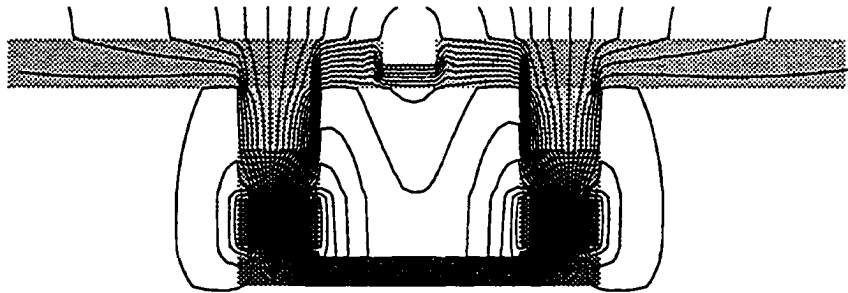


Figure 3.2: Flux contours predicted by the axisymmetric code (the brush and pipe-wall regions are scaled to show detail)

circumferential extent of the defect in meters. As can be seen from the results, the amplitude of B_z is a function of both the defect length and depth, and the time-duration of B_z is proportional, largely, only to the length of the defect. It is this relationship between the defect dimensions and signal parameters which is utilized in the MFL technique to characterize the defect.

The defects considered in this chapter are axisymmetric in nature, i.e., they have full circumferential width. However, when the defect considered is 3D in nature, the relationship between the defect and the measured signal is extremely complicated. Numerical models help provide a better understanding of the energy defect interaction, and hence are invaluable in developing accurate imaging schemes based on the

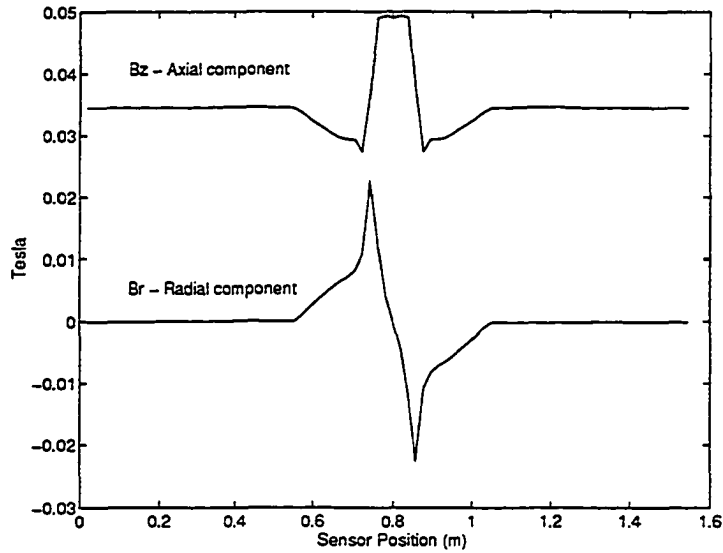


Figure 3.3: Radial and axial components of the flux density

physics of the problem.

The governing equation (Equation 3.1), does not include currents generated due to the motion of the magnetizer relative to the conductive pipe-wall. Since the magnetizer moves at speeds of up to 25 m/s , the motionally induced currents have to be included in the governing equation for accuracy of modeling. The next chapter presents an axisymmetric Galerkin formulation including velocity effects in the governing equation, and discusses the nature of velocity effects based on modeling results.

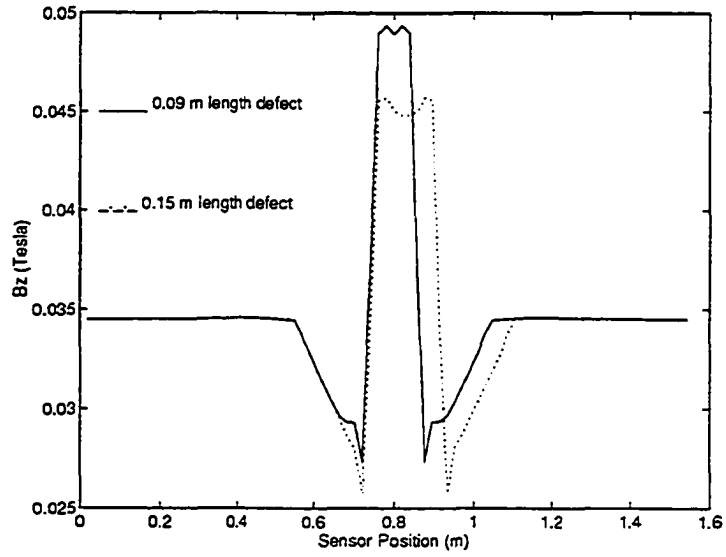


Figure 3.4: Variation of MFL signal for different defect lengths. Defect depths are 50 percent throughwall

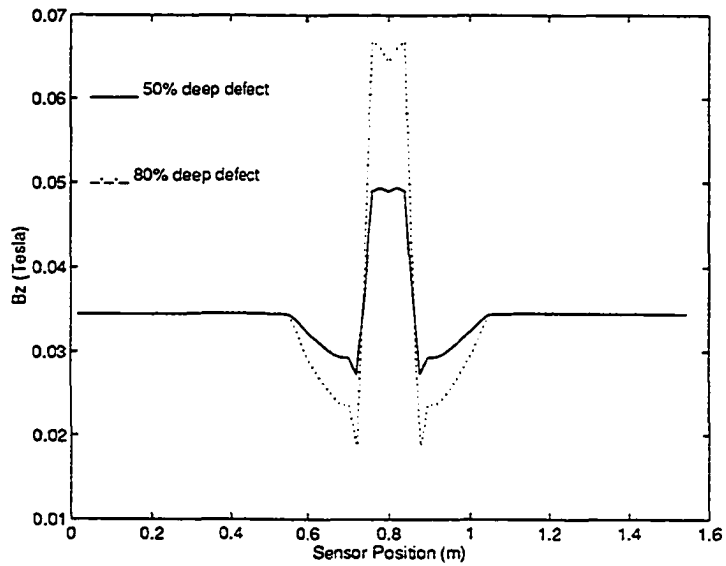


Figure 3.5: Variation of MFL signal for different defect depths. Defect widths are 0.09 m

CHAPTER 4. AXISYMMETRIC FORMULATION INCORPORATING VELOCITY

Introduction

In order to inspect large sections of pipelines in reasonable time frames, the method of inspection has to be fast. Considering the serious consequences of failure (Chapter 2), the inspection technique needs to be accurate. The MFL technique uses a magnetizer which may move at velocities up to 25 m/s . At these velocities the leakage field signal is significantly distorted due to the motionally generated currents in the pipeline. These distortions affect the accuracy of defect detection and characterization. Hence, it is important to understand and quantify velocity effects on the leakage field signal. Experimental measurements of the velocity effects are expensive and possible for only very limited choices of parameters such as geometry and dimensions of the probe, defect, etc. Analytical, closed form solutions for electromagnetic NDE problems including velocity effects can be found for only the simplest examples and are impractical for most NDE problems. Numerical analysis techniques for the modeling of velocity effects in a variety of EM areas are developing rapidly [31] - [36].

Steady state techniques, such as the upwinding technique, can be used to model velocity effects in objects of uniform geometry [36]. Since the geometry discussed in this dissertation involves a defect in the tube wall, and the position of the defect

relative to the probe varies continuously with time, the problem must be treated as one with a moving boundary. The transient nature of the process calls for the use of time stepping methods.

There are two different methods of handling the moving boundary problem, the moving coordinate method and the fixed coordinate method. In the first method, a moving coordinate system is used with the observer positioned on the object where the motion induced effect occurs. In this case, there is no motion seen by the observer except that of the field source. The field problem can be expressed and solved by the ordinary Maxwell's equations, provided that the continuously moving field source is defined. This method has the advantage that the $\mathbf{V} \times \mathbf{B}$ term responsible for spurious oscillations in fixed coordinate formulations does not appear in the governing equation. On the other hand, this approach is laborious since the motion is taken into account by a moving mesh. This generally involves extensive work in mesh regeneration or local remeshing. Recently, several methods to overcome this disadvantage have been suggested [36]. In the second method, a fixed coordinate system is used. Here, the observer has a fixed geometrical relation with the field source. A motion related term $\mathbf{V} \times \mathbf{B}$, appears in the governing equation, which results in spurious oscillations in the solution if the standard FEM methods, such as the Galerkin technique are used. However, methods to overcome these spurious oscillations have been suggested [37], [38], [39] and are discussed in the next section.

Transient Analysis of Velocity Effects

For the transient, velocity affected, electromagnetic problem, the governing equation using the magnetic vector potential (\mathbf{A}) formulation is:

$$\nabla \times \frac{1}{\mu} \nabla \times \mathbf{A} = \mathbf{J}_s - \sigma \frac{\partial \mathbf{A}}{\partial t} + \sigma \mathbf{V} \times \nabla \times \mathbf{A} \quad (4.1)$$

Compared to the standard magnetostatic governing equation (Equation 3.1), Equation 4.1 differs in including the following velocity related terms: 1) $\sigma \frac{\partial \mathbf{A}}{\partial t}$, which is the current density resulting from the changing magnetic field due to the changing spatial relationship between the defect and the source (pig); and 2) $\sigma \mathbf{V} \times \nabla \times \mathbf{A}$, which is the current density resulting from the relative motion of the magnetic field and a conductive material (pipe-wall).

For axisymmetric geometries, Equation 4.1 reduces to:

$$\frac{1}{\mu} \left[\frac{\partial}{\partial r} \left\{ \frac{1}{r} \frac{\partial(rA)}{\partial r} \right\} + \frac{\partial}{\partial z} \left\{ \frac{\partial A}{\partial z} \right\} \right] dv = \sigma \frac{\partial A}{\partial t} + \sigma V \frac{\partial A}{\partial z} - J_s \quad (4.2)$$

Several time step methods are available to solve Equation 4.2, including Donea's method [38], Zienkiewicz's method [39] and the Leismann-Frind method [37]. A detailed analysis of the comparative advantages of these methods when applied to a moving probe problem is presented in [40], and is beyond the scope of this dissertation. It has been show in [40] that the Leismann-Frind method offers superior results in terms of overall considerations of accuracy and stability for electromagnetic NDE applications. This dissertation limits itself to the application of the Leismann-Frind method to the modeling of MFL inspection of pipelines, to the axisymmetric case, and its extension for the 3D case (Chapter 7).

The finite difference method of time stepping

The Leismann-Frind method uses the finite difference approximation for time stepping. Three popular finite difference approaches are 1) the forward difference

method, 2) the backward difference method, and 3) the central difference method. In the forward difference method, each of the terms in Equation 4.2 is evaluated at time t_n (the old time level in the origin). In the backward difference scheme the terms are evaluated at time t_{n+1} (the new time level is the origin). For the central difference method the origin is midway between the old time level and the new time level i.e., at $t_n + \frac{\Delta t}{2}$. It is observed that the central difference method provides the highest accuracy and unconditional stability [40]. The expressions for magnetic vector potentials at old and new time levels, with the central difference scheme, are given by:

$$\begin{aligned}
 A^n &= A \left[\left(t_n + \frac{\Delta t}{2} \right) - \frac{\Delta t}{2} \right] \\
 &= A \left(t_n + \frac{\Delta t}{2} \right) - \frac{\Delta t}{2} \frac{\partial A \left(t_n + \frac{\Delta t}{2} \right)}{\partial t} + \frac{\Delta t^2}{8} \frac{\partial^2 A \left(t_n + \frac{\Delta t}{2} \right)}{\partial t^2} + \nu (\Delta t^3) \quad (4.3)
 \end{aligned}$$

$$\begin{aligned}
 A^{n+1} &= A \left[\left(t_n + \frac{\Delta t}{2} \right) + \frac{\Delta t}{2} \right] \\
 &= A \left(t_n + \frac{\Delta t}{2} \right) + \frac{\Delta t}{2} \frac{\partial A \left(t_n + \frac{\Delta t}{2} \right)}{\partial t} + \frac{\Delta t^2}{8} \frac{\partial^2 A \left(t_n + \frac{\Delta t}{2} \right)}{\partial t^2} + \nu (\Delta t^3) \quad (4.4)
 \end{aligned}$$

These equations are used in the Leismann-Frind formulation described in the next section.

The Leismann-Frind method for transient analysis

The Leismann-Frind method is explained using a 1D version of Equation 4.2:

$$\sigma \frac{\partial A}{\partial t} = \frac{1}{\mu} \frac{\partial^2 A}{\partial z^2} - \sigma V \frac{\partial A}{\partial z} + J_s \quad (4.5)$$

In the Leismann-Frind method, an artificial diffusion term is introduced and individual time weighting factors are used for each term in the governing equation. The artificial diffusion term and the weighting factors are determined during a process of error minimization.

Introducing an artificial diffusion term and the individual weighting factors in Equation 4.5, and using $\frac{\partial A}{\partial t} = \frac{A^{n+1} - A^n}{\Delta t}$, we obtain:

$$\begin{aligned} \sigma \frac{A^{n+1} - A^n}{\Delta t} &= \theta_d \frac{1}{\mu} \frac{\partial^2 A^{n+1}}{\partial z^2} + (1 - \theta_d) \frac{1}{\mu} \frac{\partial^2 A^n}{\partial z^2} - \theta_v \sigma V \frac{\partial A^{n+1}}{\partial z} \\ &\quad - (1 - \theta_v) \sigma V \frac{\partial A^n}{\partial z} + \theta_a \vartheta \frac{\partial^2 A^{n+1}}{\partial z^2} + (1 - \theta_a) \vartheta \frac{\partial^2 A^n}{\partial z^2} \end{aligned} \quad (4.6)$$

here, θ_d, θ_v and θ_a are the weighting factors and ϑ is the artificial diffusion term.

Now, using Equations 4.4 and 4.3 in Equation 4.6 gives:

$$\begin{aligned} \sigma \frac{\partial A}{\partial t} &= \frac{1}{\mu} \frac{\partial^2 A}{\partial z^2} - \sigma V \frac{\partial A}{\partial z} + J_s \\ &+ \left(\theta_d - \frac{1}{2} \right) \Delta t \frac{1}{\mu} \frac{\partial^2}{\partial z^2} \frac{\partial A}{\partial t} + \left(\frac{1}{2} - \theta_v \right) \sigma V \Delta t \frac{\partial}{\partial z} \frac{\partial A}{\partial t} \\ &+ \vartheta \frac{\partial^2}{\partial z^2} A + \left(\theta_a - \frac{1}{2} \right) \vartheta \Delta t \frac{\partial^2}{\partial z^2} \frac{\partial A}{\partial t} + \vartheta (\Delta t^2) \end{aligned} \quad (4.7)$$

The left-hand-side term and the first three right-hand-side terms are exactly the same as Equation 4.5, hence the remaining terms must be error terms. Rewriting the error terms using Equation 4.5, and neglecting fourth order derivative terms we get:

$$\begin{aligned} (1 - \theta_d - \theta_v) V \Delta t \frac{1}{\mu} \frac{\partial^3 A}{\partial z^3} + \left[\vartheta - \left(\frac{1}{2} - \theta_v \right) \sigma V^2 \Delta t \right] \frac{\partial^2 A}{\partial z^2} + \left(\theta_a - \frac{1}{2} \right) \vartheta \Delta t \frac{\partial^2}{\partial z^2} \frac{\partial A}{\partial t} \end{aligned} \quad (4.8)$$

Based on observation of the effect of the $\frac{\partial A}{\partial t}$ term, it is concluded that it has to be evaluated only at the old time level. From an examination of Equation 4.6, it is apparent that for this to be possible, θ_v has to be zero. Also, in Equation 4.8, all the individual coefficients must equal zero. Hence, we obtain $\theta_d = 1$, and $\vartheta = \frac{\sigma V^2 \Delta t}{2}$. The value of θ_a is decided by stability analysis. It is shown that stability can be achieved if $\theta_a \geq \frac{1}{3}$ and unlimited stability is guaranteed when $\theta_a \geq \frac{1}{2}$. Finally, substituting these values for the weighting factors and the artificial diffusion term into Equation 4.7 we get the final form of the Leismann-Frind equation for the 1D case:

$$\begin{aligned} & \left[\frac{\sigma}{\Delta t} - \frac{1}{\mu} \frac{\partial^2}{\partial z^2} - \theta_a \frac{\sigma V^2 \Delta t}{2} \frac{\partial^2}{\partial z^2} \right] A^{n+1} \\ &= J_s + \left[\frac{\sigma}{\Delta t} + (1 - \theta_a) \frac{\sigma V^2 \Delta t}{2} \frac{\partial^2}{\partial z^2} - \sigma V \frac{\partial}{\partial z} \right] A^n \end{aligned} \quad (4.9)$$

Using the Galerkin approach described in Chapter 3, the finite element formulation of Equation 4.9 (modified for the axisymmetric case) is:

$$\begin{aligned} & \sum_{i=1}^k \int_s \left(\frac{\sigma}{\delta} N_j N_i A_i^{n+1} \right) ds + \int_s \left(\frac{1}{\mu} \frac{\partial N_j}{\partial r} \frac{\partial N_i}{\partial r} A_i^{n+1} \right) ds - \oint_c \left(N_j \frac{\partial A_i^{n+1}}{\partial r} \right) dc \\ &+ \int_s \left(\frac{1}{\mu r} N_j \frac{\partial N_i}{\partial r} A_i^{n+1} \right) ds + \int_s \left(\frac{1}{\mu r} N_i \frac{\partial N_j}{\partial r} A_i^{n+1} \right) ds + \int_s \left(\frac{1}{\mu} \frac{\partial N_j}{\partial z} \frac{\partial N_i}{\partial z} A_i^{n+1} \right) ds \\ &- \oint_c \left(N_j \frac{\partial A_i^{n+1}}{\partial z} \right) dc - \int_s \left(\frac{1}{\mu r^2} N_j N_i A_i^{n+1} \right) ds + \int_s \left(\frac{1}{2} \frac{\sigma V^2 \delta}{2} \frac{\partial N_j}{\partial z} \frac{\partial N_i}{\partial z} A_i^{n+1} \right) ds \\ &= \sum_{i=1}^k \int_s \left(\frac{\sigma}{\delta} N_j N_i A_i^n \right) ds - \int_s \left(\frac{1}{2} \frac{\sigma V^2 \delta}{2} \frac{\partial N_j}{\partial z} \frac{\partial N_i}{\partial z} A_i^n \right) ds - \int_s \left(\sigma V N_j \frac{\partial N_i}{\partial z} A_i^n \right) ds \\ & \quad + \int_s (N_j \mathbf{J}_s) ds = 0 \end{aligned} \quad (4.10)$$

The procedure is carried out for all nodes until j is the maximum number of nodes.

The FEM technique is now applied to the geometry show in Figure 3.1. The results and analysis are presented in the following section.

Results and Analysis

Figure 4.1 shows the effect of velocity on the flux lines in the vicinity of the magnetizer. The effect is to distort the flux lines by dragging them behind as the tool moves forward. The effect of velocity on the axial component (\mathbf{B}_z) of the leakage field signals is shown in Figure 4.2. Two distinct effects are observable, one is the gross reduction of the magnetization level, and the second is the distortion of the signal in the defect region. The reduction of the magnetization level is explained to be a result of motion induced distortion of the magnetizer field as shown in the flux plots of Figure 4.1 (compare with the static case in Figure 3.2). This distortion of the magnetizer field is in-turn due to the circumferential currents induced by the magnet poles. Figures 4.3 and 4.4 compare the axial and radial components of \mathbf{B} (directly under the magnetizer poles) for the static case and the case with the magnetizer moving at 5 m/s. The large radial component of \mathbf{B} under the poles, which is perpendicular to the direction of motion, results in large currents in the pipe-wall in the vicinity of the poles. As seen in Figure 4.4, the peak value of the radial component is 0.8 Tesla. Assuming approximately similar levels of \mathbf{B}_r in the pipe-wall, in the vicinity of the poles, the corresponding value of induced currents when the magnetizer is moving at 5 m/s is, $\sigma \mathbf{V} \times \mathbf{B} = 24 \times 10^6 A/m^2$. These currents produce fields which oppose the original fields, hence distorting and reducing the magnetization level. The reduction of magnetization levels produces smaller MFL

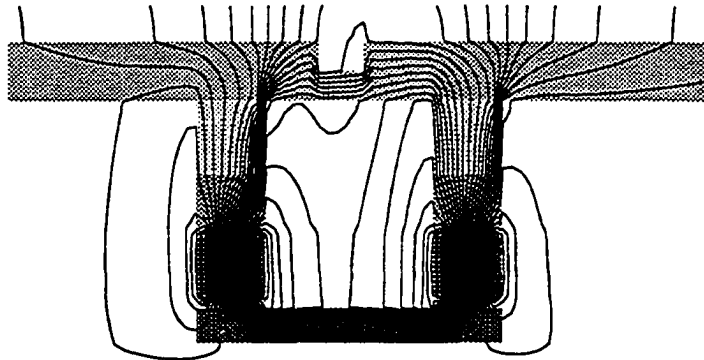


Figure 4.1: Velocity effects on the flux lines at 5 m/s, defect is 0.09 m long and 50 percent through wall (the brush and pipe-wall regions are scaled to show detail)

signals for the same defect with increasing velocities. This behavior confuses defect characterization schemes, as it replicates the behavior of MFL signals corresponding to different depths (Figure 3.5).

The analysis of the distortion in the defect region requires a deeper study. Figure 4.5 shows a plot of the induced currents in the vicinity of the defect. The magnitudes of the currents for an axial scan line directly below the defect are shown in Figure 4.6. These currents are termed defect induced currents. The presence of the defect results in a radial component of the field at the edges of the defect. The radial component of the field at the defect edges changes in magnitude as the magnetizer moves across the defect. This changing radial component of the field, which is perpendicular to the direction of motion, results in defect induced currents. These currents distort the leakage field signals. Defect induced currents are in opposite directions (as shown in Figure 4.5) at each edge depending on the direction of the magnetizer field. They have the effect of adding and subtracting from the leakage field signal and thus skewing it.

The application of the code to tool design is now considered. Since the net effect

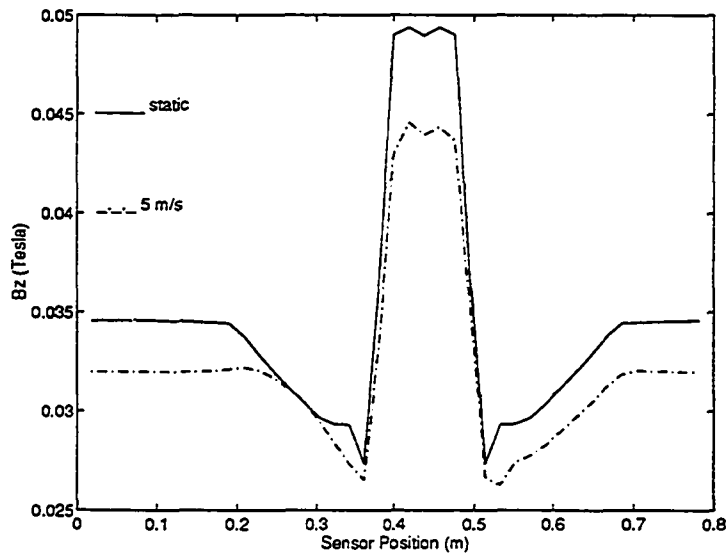


Figure 4.2: Variation of MFL signal with velocity. Defects are 0.09 m long and 50 percent through wall

of velocity on the flux lines is to drag them as shown in Figure 4.1, a compensation can be envisioned, where an asymmetric magnetization is set up to counter the dragging effect. A simple manner in which this can be achieved is by removing the magnet in the trailing pole-piece of the magnetizer. This refers to the magnet on the right in Figure 3.1 (considering the magnetizer to be moving from the left to the right). The magnet is replaced by ferromagnetic material to provide a closed magnetic path. Results obtained by simulating this geometry, and subtracting signal base levels, are shown in Figure 4.7. As can be seen even for a large variation of velocity, relatively small velocity effects are observed. It should be pointed out that this result is obtained for the defect with the smallest length of interest (0.05 m long). The velocity effects are the higher for defects with smaller lengths, hence this compensation scheme works even better for larger defects.

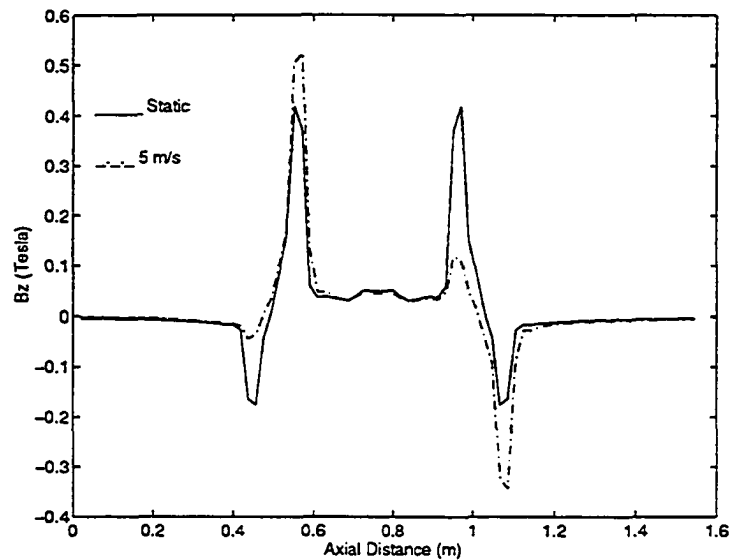


Figure 4.3: Comparison of the values of the axial component of the flux density under the poles

The code is also used to demonstrate the differences between transient analysis and steady-state analysis. Reference [40] shows that the results obtained with the upwinding technique matched those from the Leismann-Frind method, if the transients at each time step in the Leismann-Frind method were allowed to die away, by iterating at each time step until convergence was reached. Using this observation, the difference between the upwinding technique and the transient analysis approach are shown in Figures 4.8 - 4.10. These results clearly demonstrate the need for transient analysis in modeling motion-related NDE phenomena.

Summarizing, this chapter describes how velocity effects are incorporated into the numerical model, and uses the resulting formulation to simulate and discuss motion-related NDE problems in detail. The results presented in this chapter are obtained ignoring the effects of permeability on the resulting signals. The following

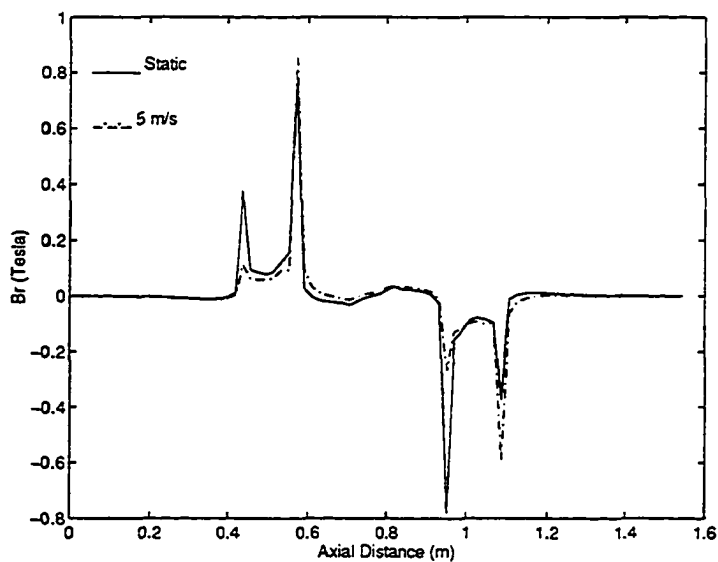


Figure 4.4: Comparison of the values of the radial component of the flux density under the poles

chapter discusses the nature and the extent of permeability effects, in NDE applications, and presents a method of incorporating permeability effects into the model. The need to incorporate permeability is justified using the results obtained.

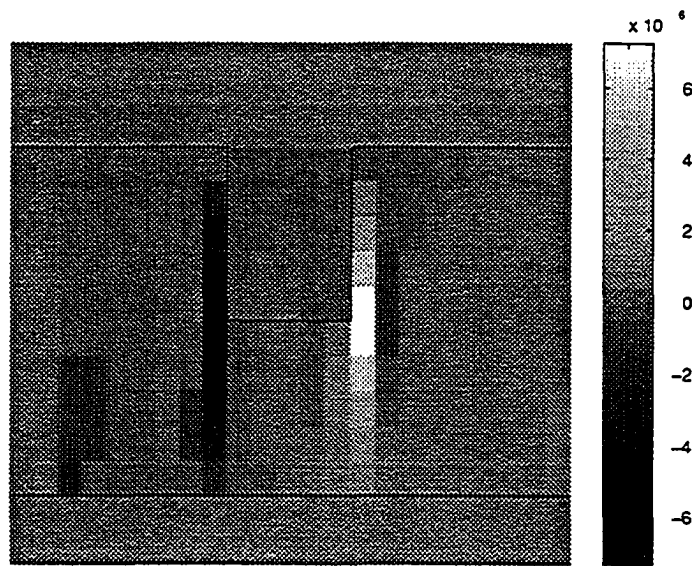


Figure 4.5: Distribution of induced currents at defect edges. Defect is 0.09 m long and 50 percent through wall, and magnetizer velocity is 5 m/sec (scale indicates magnitudes in A/square-meter)

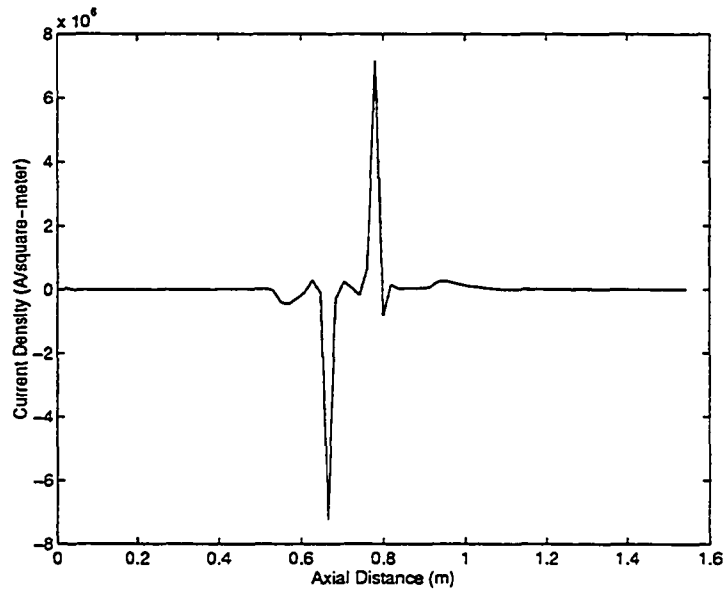


Figure 4.6: Magnitude of induced currents under the defect. Defect is 0.09 m long and 50 percent through wall, and magnetizer velocity is 5 m/sec

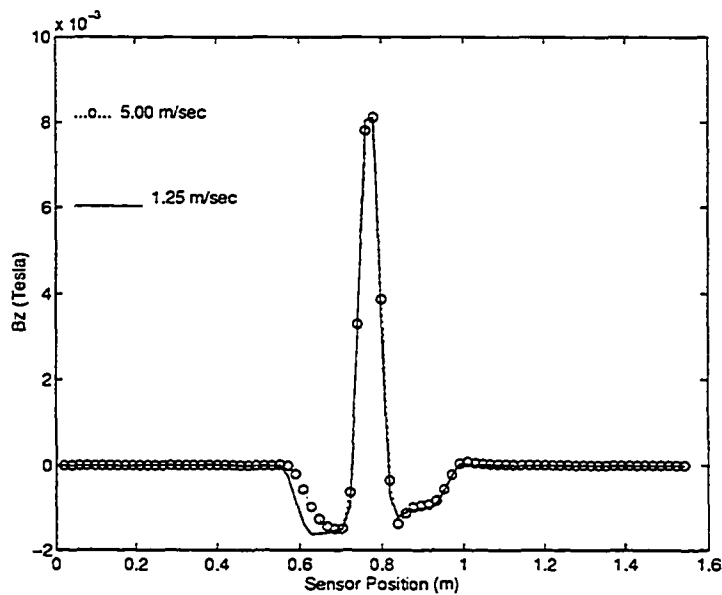


Figure 4.7: Velocity effects for a .05 m long, 50 percent through wall defect with the modified tool

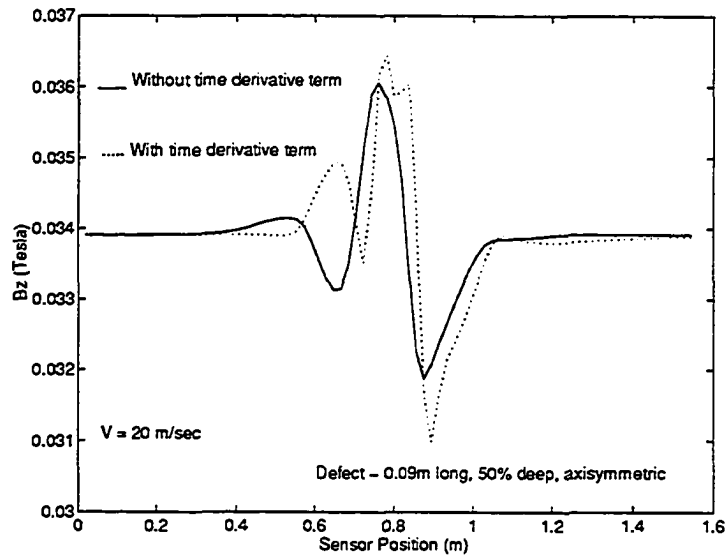


Figure 4.8: Comparison of transient and static analysis for a 0.09 m long 50 percent through wall defect

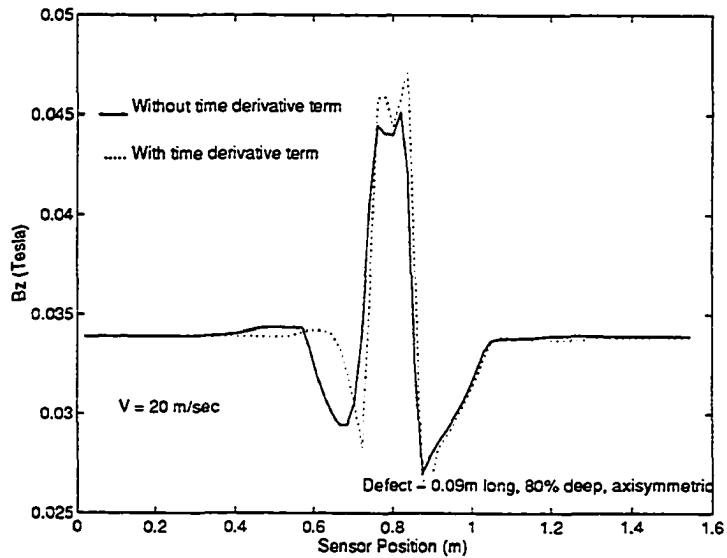


Figure 4.9: Comparison of transient and static analysis for a 0.09 m long 80 percent through wall defect

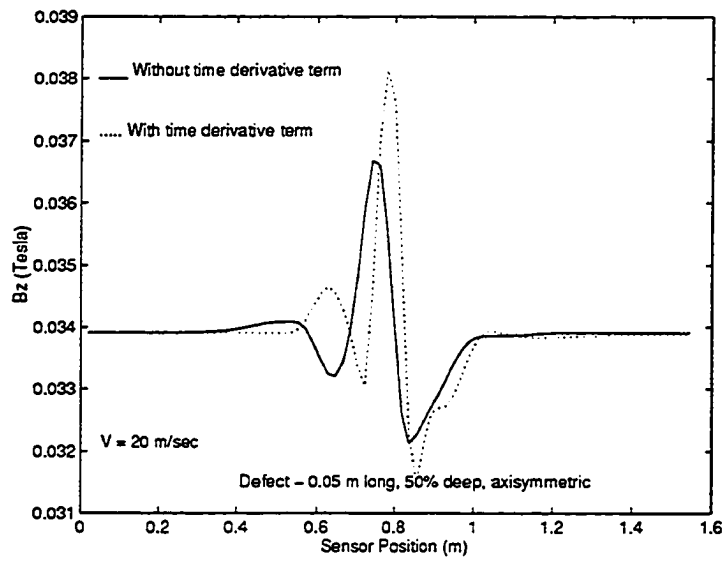


Figure 4.10: Comparison of transient and static analysis for a 0.05 m long 50 percent throughwall defect

CHAPTER 5. NONLINEAR ANALYSIS INCORPORATING PERMEABILITY EFFECTS

Introduction

Thus far, the nonlinear nature of permeability for the ferromagnetic parts has been ignored. The ferromagnetic parts are assumed to be operating in the linear region of the BH curve. However, this assumption does not hold in practice since the operating point of the ferromagnetic parts varies considerably, with both the backing iron and the pipe-wall being driven to saturation. In this chapter, an algorithm is presented to model nonlinear permeability (assuming constant permeability within each element). Permeability variations in the vicinity of the defect are particularly important since they directly influence the leakage field signal. An existing 3D magnetostatic scalar-potential code, capable of modeling situations where velocity effects are negligible, is used to study the variations of permeability in the vicinity of the defect. This study confirms the importance of modeling nonlinear permeability and, in addition, presents the need for modeling the given geometry in full 3D for quantitatively accurate results. As part of this study both the axisymmetric and 3D codes used are validated.

Iterative Solution of Nonlinear Equations

Several methods are available for solving problems with nonlinearity of permeability. Newton's method and its variations [41], secant methods [42], modification methods [43], continuation methods [44], and generalized linear methods [45] are popular. The method used in this work falls into the category of the generalized linear methods and is discussed next.

In the algorithm used, an initial linear run of the finite element code is performed to obtain initial \mathbf{B} magnitudes. The magnitude of \mathbf{H} for each element is calculated using two sample points on the BH curve closest to the initial \mathbf{B} magnitude (Figure 5.1:

$$H = H_1 + [H_2 - H_1] \left[\frac{B - B_1}{B_2 - B_1} \right] \quad (5.1)$$

where B is the initial magnitude of \mathbf{B} for the current element; B_1 and B_2 are the sample magnitudes of \mathbf{B} on the BH curve closest to B , where $B_1 < B < B_2$; H_1 and H_2 are the magnitudes of \mathbf{H} , on the BH curve, corresponding to B_1 and B_2 respectively. This is a linear interpolation scheme. The reluctivity ν is now computed ($\nu = \frac{H}{B}$). This value of ν is used to update the reluctivity using $\nu_{new} = (\nu - \nu_{old}) \nu_{fac} + \nu_{old}$, where ν_{fac} controls the convergence rate. This calculation is performed on all elements. Using the new set of reluctance values, the finite element formulation computes the new values of \mathbf{A} and hence \mathbf{B} . Convergence is reached when the value of \mathbf{A} remains constant for each element, within specified tolerance limits, over subsequent iterations.

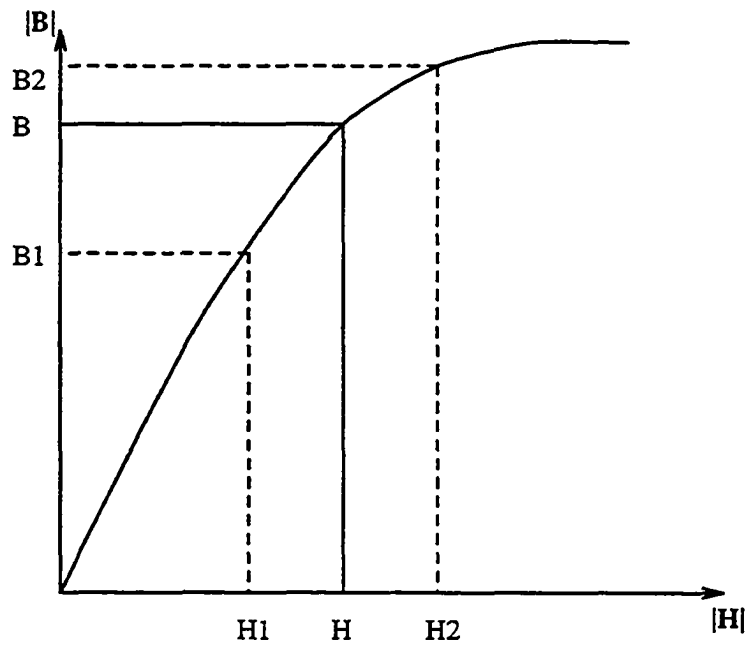


Figure 5.1: Operating points on the initial BH curve

Application of the Nonlinear Formulation

In this section results from nonlinear formulations are presented. Also, a study of the differences between axisymmetric and 3D geometries is presented based on an understanding of permeability variations around a defect.

The two formulations used in this investigation are summarized below:

Axisymmetric formulation

For the axisymmetric geometry, the magnetic vector potential (\mathbf{A}) formulation is used. Starting from Maxwell's equations the governing equation derived is:

$$\nabla \times \frac{1}{\mu} \nabla \times \mathbf{A} = \mathbf{J}_s \quad (5.2)$$

This equation is simplified for the axisymmetric case and solved using finite element (FE) techniques as described in Chapter 2.

3D formulation

The governing equation for the 3D formulation makes use of the magnetic scalar potential ψ . The equation solved is Poisson's equation:

$$\nabla \cdot \mu \nabla \psi = -\rho_m \quad (5.3)$$

where $\rho_m = -\nabla \cdot \mathbf{B}_{rem}$ is referred to as the "magnetic charge density" (\mathbf{B}_{rem} is the remanent magnetization of the material). This method of approximating a permanent magnet using magnetic charge density is valid for the neodymium magnets used in the pig, since they exhibit highly linear relaxation curves.

Results and analysis

As the study reported in this chapter is quantitative in nature, a validation of the numerical models is extremely important. The FE codes were validated by comparing numerical predictions with experimental results. Experimental results include measured values of the static axial (\mathbf{B}_z), and radial (\mathbf{B}_r) components, for an axial scan line directly above the pipe-wall, in the vicinity of the magnetizer. The geometries considered are: (1) the magnetizer placed in the pipe, and (2) the magnetizer placed in air (the scan line being at a lift-off equal to the pipe-wall thickness).

Typical results showing excellent comparison between FEM solutions and the experimental scans are presented in Figure 5.2 and Figure 5.3. Since the geometry of the magnetizer for which these tests were performed is 3D (corresponding to Figure

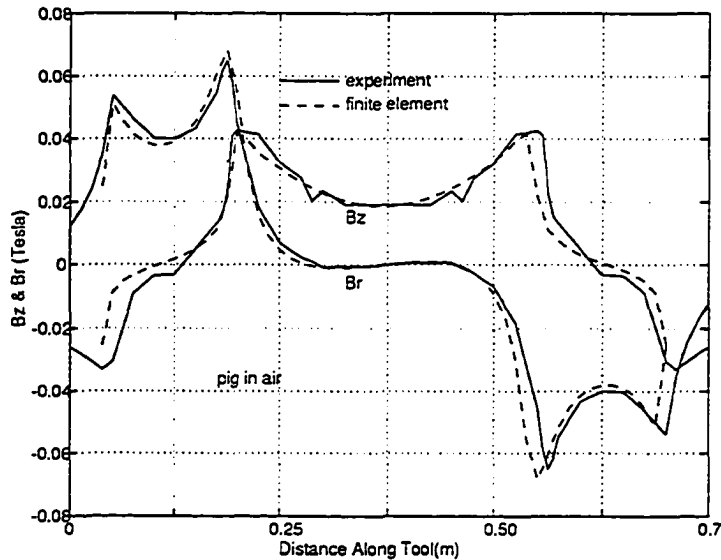


Figure 5.2: Comparison of experimental and FEM results with the magnetizer placed in air

2.2 b), the 3D code is used in these comparisons. The axisymmetric code is validated by comparing results with the validated 3D code as described next.

The first step in this investigation is to analyze MFL signals from an axisymmetric defect with an axisymmetric magnetizer. The dimensions of the axisymmetric defect used in this chapter are - 0.1m length (axial dimension), 40% through wall depth, full circumference width (circumferential dimension). This defect is a typical “critical” defect in the pipeline industry. Figure 5.4 shows the MFL signals obtained using the axisymmetric code and the 3D code. As expected, the solutions from both the codes match with negligible error.

Next, the 3D magnetizer and an axisymmetric defect are modeled. In this case, the signal obtained (Figure 5.5) is seen to be much lower (approximately 50%) than with an axisymmetric magnetizer. From an analysis of the two geometries, the large

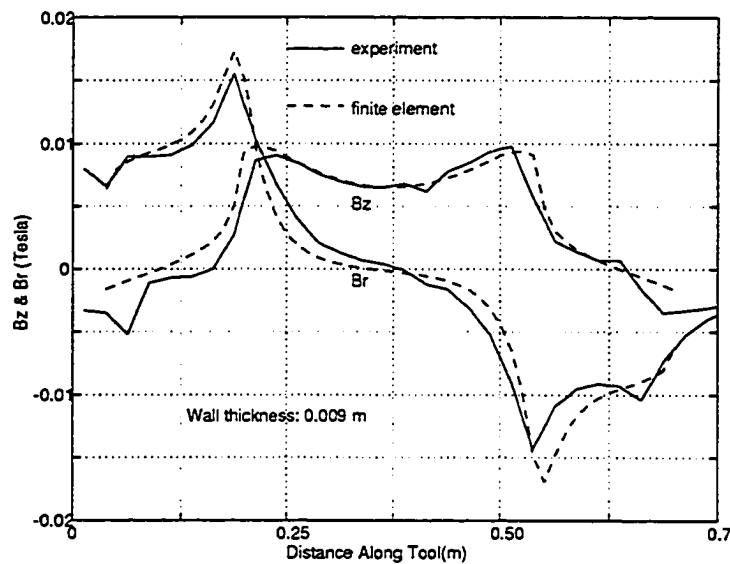


Figure 5.3: Comparisons of experimental and FEM results with the magnetizer place in a pipe

variation in signal levels between the axisymmetric magnetizer and the 3D magnetizer, can be attributed to the differences in the saturation of the pipe-wall under the defect. The pipe-wall under the defect with the axisymmetric magnetizer is under higher saturation relative to the 3D magnetizer resulting in increased leakage fields.

Figure 5.6 shows the signals obtained for a 3D defect with an axisymmetric magnetizer. For the 3D defect, the dimensions are - 0.1m length, 40% depth and 0.2m width. The 3D defect and the axisymmetric defects are exactly the same, other than for the circumferential width. Figure 5.7 shows the signals obtained for a 3D defect with a 3D magnetizer. There is approximately a 50% reduction in signal levels with a 3D defect compared to signal levels with an axisymmetric defect. Again, the saturation of the pipe-wall under the defect is a key factor governing the differences in the signal levels.

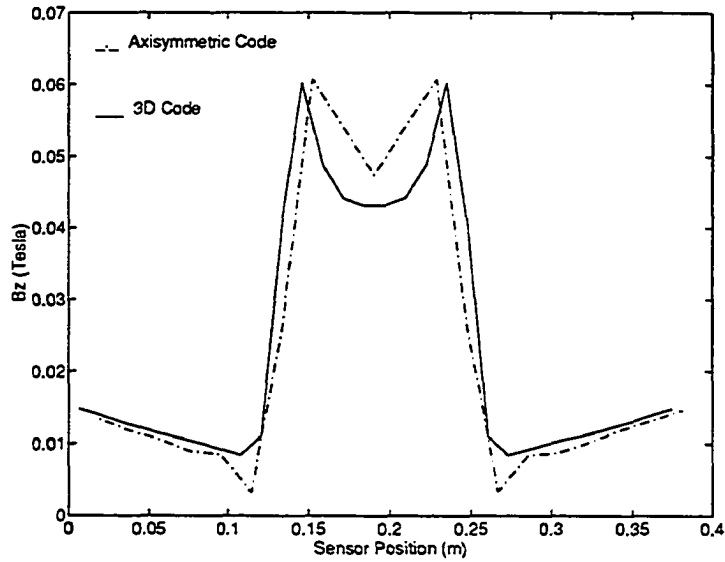


Figure 5.4: Comparison of codes - axisymmetric defect and axisymmetric magnetizer

To support the arguments presented above, typical variation of relative permeability around the defect for the axisymmetric and the 3D cases are presented in Figure 5.8 and Figure 5.9 respectively. The relative permeability under the defect for the axisymmetric magnetizer with the axisymmetric defect is of the order of 10 and for the 3D magnetizer with the 3D defect of the order of 100. It is evident that the region of the pipe-wall under the defect in the axisymmetric case is under very high saturation (permeability close to that of air). For the 3D magnetizer there is considerable fringing of the EM field in between the magnet-assembly sections. For a 3D defect, flux lines redistribute themselves under and around the defect. In contrast, the flux lines are all forced under the defect sending this region into high saturation in the case of an axisymmetric defect.

In summary, this chapter compares 3D and axisymmetric geometries of the MFL

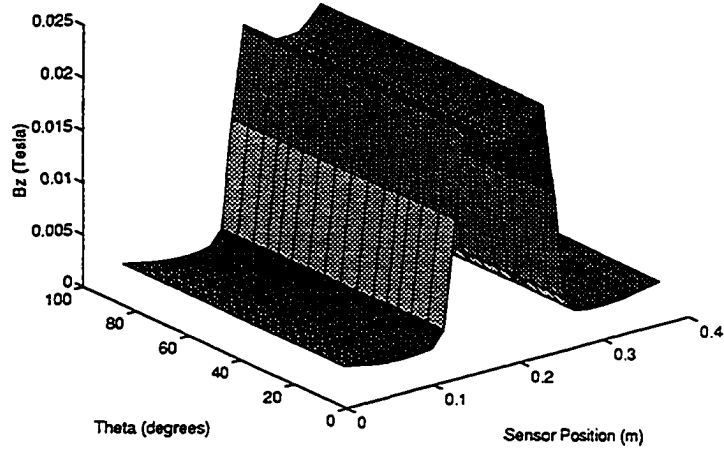


Figure 5.5: MFL signal from axisymmetric defect with a 3D magnetizer

magnetizer. The signals obtained in the case of the axisymmetric magnetizer are observed to be much larger than those obtained with the 3D magnetizer. This is attributed to the observation that the region under the defect is under much higher saturation in the axisymmetric case. Higher saturation under the defect in the axisymmetric case, also results in reduced sensitivity to defect depth. The complex nature of the field distribution in the pipe-wall for 3D defects indicates the need to use 2D leakage field scans for accurate defect characterization. The typically used 1D leakage signals (discussed in Chapter 3) are appropriate for the characterization of axisymmetric defects. Another conclusion from the results presented in this chapter is that, for obtaining quantitatively reasonable results, the geometry being investigated has to be modeled in its entirety. Axisymmetric approximations can be used to provide a quick qualitative understanding of the basic phenomena involved. The following chapter applies the axisymmetric numerical model incorporating nonlinear-

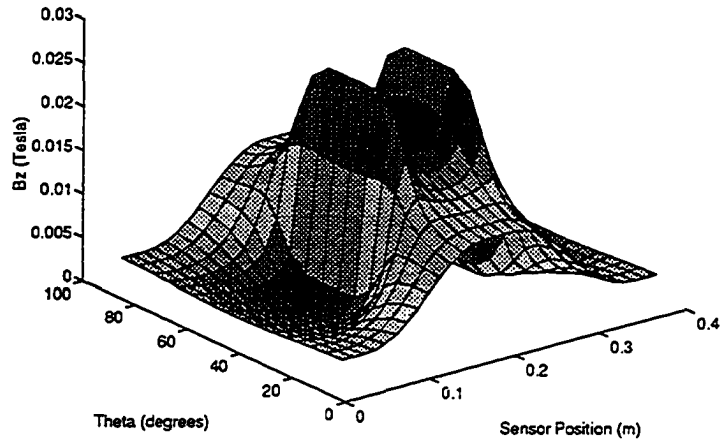


Figure 5.6: MFL signal from 3D defect with an axisymmetric magnetizer

ity and velocity effects to investigate the presence of additional modalities associated with the pig, in order to demonstrate the usefulness of the model.

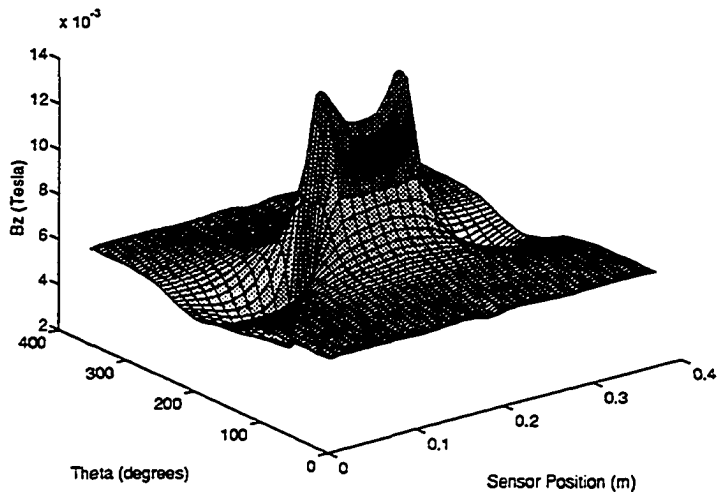


Figure 5.7: MFL signal from 3D defect with a 3D magnetizer

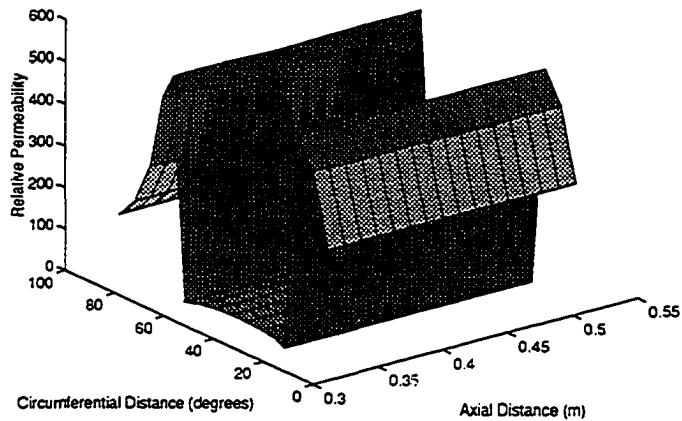


Figure 5.8: Permeability distribution under an axisymmetric defect with an axisymmetric magnetizer

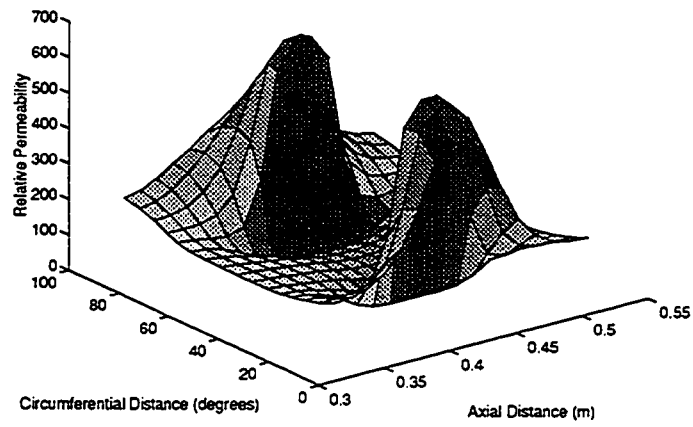


Figure 5.9: Permeability distribution under a 3D defect with a 3D magnetizer

CHAPTER 6. APPLICATIONS OF THE NONLINEAR AXISYMMETRIC CODE INCORPORATING VELOCITY

Introduction

This chapter demonstrates the usefulness of the nonlinear axisymmetric code incorporating velocity. This objective is achieved by using the numerical model to study the possibility of taking advantage of alternative modalities associated with the standard magnetic flux leakage tool to obtain additional defect information. Since the MFL inspection technique is static in nature, the information content present in an MFL signal is typically less than signals from AC methods such as eddy-current and wave based NDE techniques. It is therefore of interest to determine if supplementary information relating to the condition of the pipe can be gained by exploiting additional physical processes that are initiated by the inspection vehicle.

As mentioned earlier, the inspection vehicle moves with velocities up to 25 m/s . The results presented in this chapter show that under these conditions, in addition to the standard MFL signals, a wealth of information relating to the condition of the pipe is generated by the different modalities associated with the inspection vehicle. The additional physical processes that can be exploited include: (1) the motionally induced remote field eddy current (RFEC) effect [35], (2) motionally induced currents at defect edges, (3) variable reluctance (VR) effect, (4) defect perturba-

tion of motionally induced circumferential currents at poles (discussed in Chapter 4), and (5) residual leakage fields. Information associated with these modalities can be tapped using the existing inspection vehicles without major modifications. Since these modalities are governed by different physical processes, they are expected to be sensitive to different defect types. The critical nature of gas pipeline inspection calls for an in-depth study of the defect information present in these modalities. This dissertation investigates the first three modalities using results obtained from numerical simulations in order to illustrate the usefulness of the nonlinear axisymmetric code incorporating velocity effects.

Additional Modalities for Pipeline Inspection

Two major factors determine if a particular NDE method is useful for a given application: (1) the detectability of the signal produced due to the energy-defect interaction, and (2) the sensitivity of the signal to small variations in the defect dimensions. The signal obtained is required to have high signal to noise ratio (SNR) for it to be useful in defect detection applications. The dimension of the critical flaw (the smallest defect of interest) determines the minimum signal amplitudes for the method to meet the SNR requirements. Also, for good defect characterization, small variations in defect dimensions should produce measurable variations in the signal obtained (in the range of defect dimensions of interest). Again, the resolution required by the application determines which method is best suited for defect characterization. Typically, there is a trade-off between the two factors, described above, in deciding evaluating an NDE method.

In the following paragraphs, results showing the detectability and sensitivity of

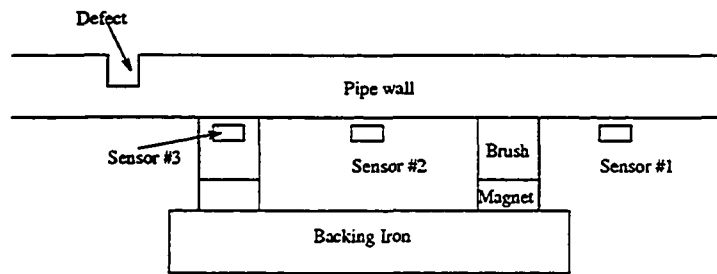


Figure 6.1: Sensor positions associated with the additional modalities

each of the modalities are presented. For the sake of completeness, the MFL method is also summarized. The geometry of the magnetizer showing the sensor locations associated with the various modalities is presented in Figure 6.1

Standard MFL

The presence of a defect in a magnetized ferromagnetic material results in a redistribution of magnetic field in the vicinity of the flaw, causing some of the magnetic field to “leak” out into the surrounding medium. This leakage field can be detected, using Hall element sensors to measure the axial or radial components of the magnetic flux density B [24] (a detailed discussion is provided in Chapter 2). Typical axial components of MFL signals obtained for the geometry corresponding to Figure 6.1 are shown in Figure 6.2. The axial defect dimension is specified in the figure, and the depth of all defects studied in this chapter are 50% throughwall. The MFL signals are measured by sensor #2, placed at the center of the magnetizer (Figure 6.1). These signals are a measure of the fields which leak out from under the defect. The width of the signal is proportional to the defect length (axial dimension) and the amplitude of the signal is proportional to both the length and depth of the defect (as discussed

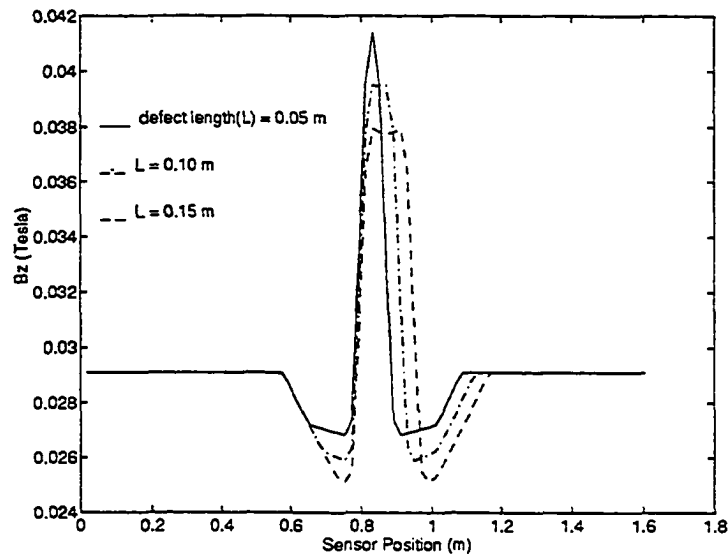


Figure 6.2: Typical MFL signals

in Chapter 3). The signal amplitudes, as shown, are clearly measurable using Hall element sensors.

Variable reluctance

The VR probe has been previously used in detecting the presence of magnetite and denting of steam generator tubes in pressurized water reactors [46], [47]. A typical VR probe consists of a simple bobbin with a DC excitation winding and a Hall element plate mounted on the periphery of the bobbin. A similar arrangement is possible with the MFL inspection vehicle, by placing a sensor in brush region of the magnetizer (sensor #3 in Figure 6.1). The basic premise is that, reluctance variations resulting from the presence of a defect, can be monitored directly by measuring the flux through the magnetic circuit. Figure 6.3 shows signals obtained from sensor #3 and are a measure of the change in reluctance of the magnetic circuit formed by the

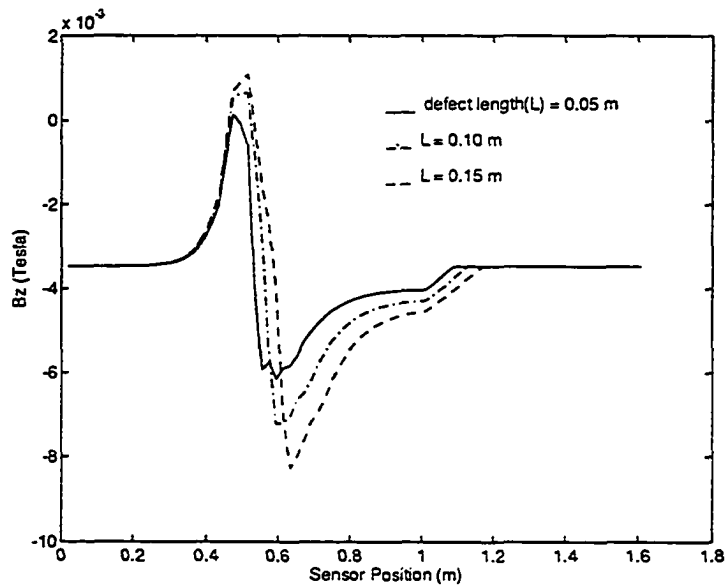


Figure 6.3: Typical VR signals

inspection vehicle and the pipe-wall in the presence of a defect. The cross-over points of the signal are proportional to the defect width and the amplitude of the signal is proportional to both the defect length and depth. These signals have much lower amplitudes compared to the MFL signals. However, the signal amplitudes are still in the measurable range for Hall element sensors.

Motion induced RFEC

RFEC probes have been successfully used in the measurement of wall thickness of oil well casing and pipelines; and are also capable of detecting pits and cracks [48] - [52]. Typically, the RFEC effect is observed in the presence of AC fields [50]. Research shows [51] that the effect is characterized by a bi-directional transmission of EM field energy through pipe-walls. The eddy currents generated by AC fields are

responsible for the bi-directional transmission of the EM field. In the case of a moving DC field, the RFEC effect has been observed [35] and is produced by the motionally induced eddy currents. Though currents induced at the poles and at the defect both produce an independent RFEC, the large currents produced at the poles dominate the effect described in this section. The bi-directionally transmitted signal, for classical RFEC, can be detected approximately two to three pipe-diameters away from the transducer. In the case of motionally induced RFEC, good detection is obtained by placing the sensor about one pipe-diameter from the magnetizer (sensor #1 in Figure 6.1). Figure 6.4 shows the signals obtained from sensor #1. Two peaks are observed from the plot, the first peak occurring when the pole piece of the magnetizer (closer to sensor #1) passes under the defect and the second peak when sensor #1 passes under the defect. The signal picked up by the sensor when the defect is in the vicinity of the pole piece is the RFEC signal, and is picked up after bi-directional transmission of EM field energy through the pipe-walls. This behavior is identical to a traditional RFEC tool excited by AC current. As can be observed from the results, the signals vary significantly with changing defect dimensions. However, the signal amplitudes are lower than those obtained with both the MFL and VR modalities, but still in a measurable range for Hall element sensors.

Motion induced currents at defect edges

The defect edges force a \mathbf{B} component perpendicular to the direction of motion 4.1. The presence of this radial \mathbf{B} component induces currents at the defect edges (Figure 6.5). The currents at each edge are in opposite directions. Hence, the currents skew the peak of the MFL signal (Figure 6.6) which is measurable and thus contain

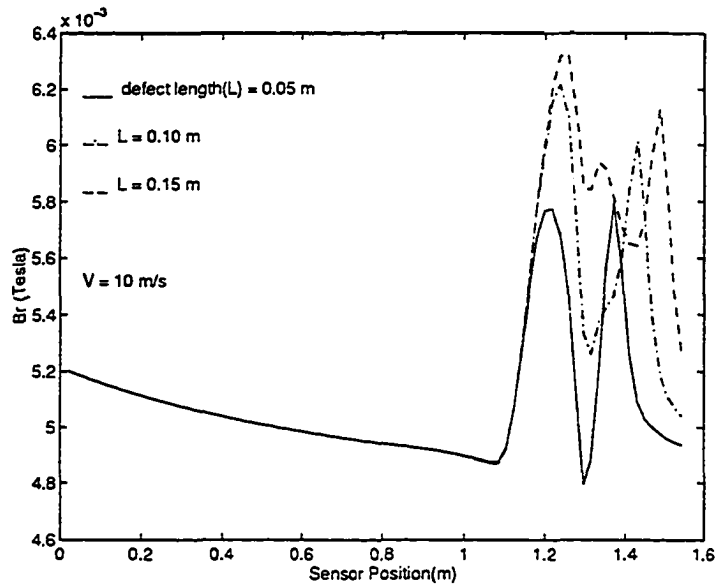


Figure 6.4: Typical RFEC signals

extractable defect information.

In conclusion, this chapter clearly demonstrates the versatility of the axisymmetric velocity effect code to study energy-defect interactions. Results presented show conclusively that there are several untapped modalities associated with the MFL inspection vehicle. Additional information obtained from the VR modality and the defect induced currents can enhance the defect characterization capability of the inspection system. The motion induced RFEC modality offers two important advantages (to be verified): (a) equal sensitivity to defects on both sides of the pipe-wall due to the bi-directional transmission of the EM field, and (b) high sensitivity to axial cracks due to the orientation of the generated fields - overcoming a major disadvantage in the MFL inspection technique. Much work is yet to be completed before these modalities can be tapped in a useful manner. The VR signals are highly sensi-

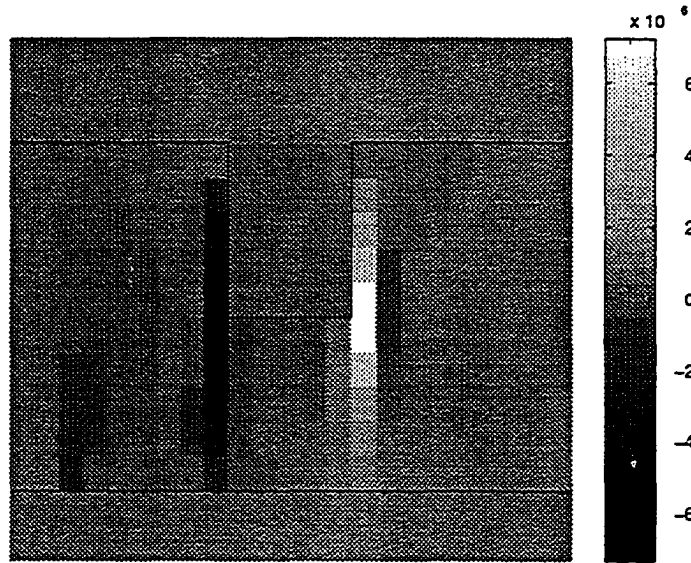


Figure 6.5: Currents at defect edges

tive to velocity effects (Figure 6.7). Hence, effective schemes to compensate velocity effects are essential before using VR signal data in defect characterization. Also, the defect induced currents are largely dependent on the shape of the defect, and under some conditions the amplitudes are not large enough to enable extraction of defect information.

The results presented in chapter are obtained using the axisymmetric model incorporating velocity and permeability effects. However, as shown in Chapter 5, 3D modeling is necessary in order to provide qualitatively accurate results for realistic defects. The following chapter discusses methods of 3D modeling of magnetostatic phenomena, incorporating velocity effects. A new technique with edge-based finite elements is developed and validated by comparing results with experimental results and other numerical techniques.

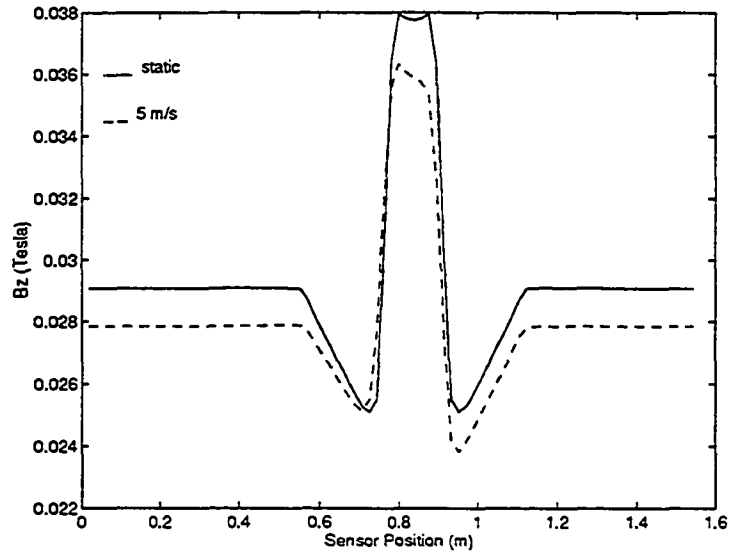


Figure 6.6: Skewing of the MFL signal due to induced currents at defect edges

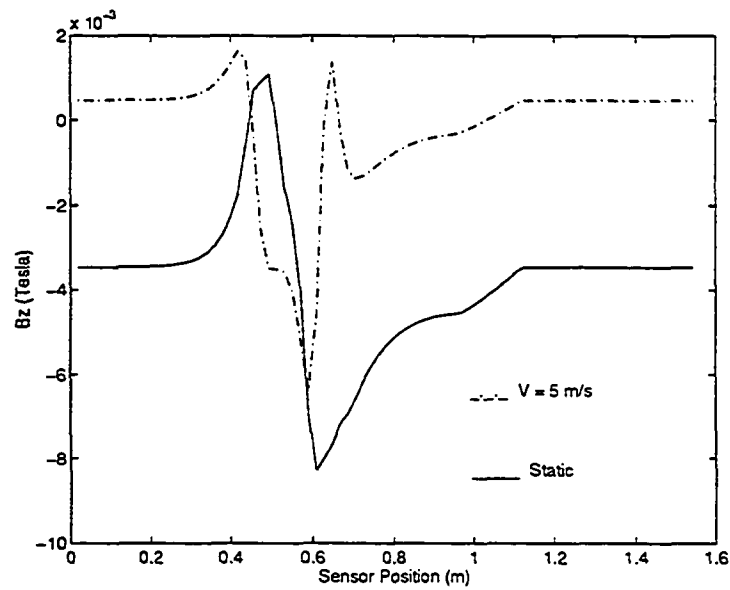


Figure 6.7: The effect of velocity of VR signal. Defect is 0.15 m long

CHAPTER 7. THREE-DIMENSIONAL MODELING OF VELOCITY EFFECTS

Introduction

So far, we have formulated the finite element method assuming axisymmetry. Even in cases where the magnetizer is truly axisymmetric, the axisymmetric formulation is not valid for modeling realistic 3D defects. As demonstrated in Chapter 6, a 3D formulation is necessary in order to make quantitatively realistic predictions of MFL signals. However, in 3D formulations several problems are encountered in dealing with motion related problems. This chapter investigates the problems associated with classical node-based FEM techniques, when applied to 3D magneto-static motion-related problems. This chapter demonstrates how the use of edge-based FEM techniques overcome these problems. The 3D formulation for the magneto-static motion-related problem is developed using transient analysis techniques. The corresponding Galerkin finite element formulation is presented. The details of implementing the edge element based mesh generator and the finite element solver are included. Results obtained using the edge element code are presented and discussed.

A-V Formulation

In the previous chapters the MVP formulation has been used in conjunction with nodal elements to provide an axisymmetric solution. The MVP formulation is derived from the more general A-V formulation, discussed below:

Using the definition of \mathbf{A} ($\mathbf{B} = \nabla \times \mathbf{A}$) and Faraday's law for the time varying case ($\nabla \times \mathbf{E} = -\frac{\partial \mathbf{B}}{\partial t}$), we get,

$$\nabla \times \left(\mathbf{E} + \frac{\partial \mathbf{A}}{\partial t} \right) = 0. \quad (7.1)$$

Using the vector identity $\nabla \times \nabla \phi = 0$, where ϕ is any arbitrary scalar quantity, we obtain,

$$\mathbf{E} = - \left(\frac{\partial \mathbf{A}}{\partial t} + \nabla \mathcal{V} \right) \quad (7.2)$$

where \mathcal{V} is a scalar potential. Neither \mathbf{A} nor \mathcal{V} are completely defined since the gradient of an arbitrary scalar function can be added to \mathbf{A} and the time derivative of the same function can be subtracted from \mathcal{V} without affecting the physical quantities \mathbf{E} and \mathbf{B} . These changes to \mathbf{A} and \mathcal{V} are the so-called gauge transformations, and the uniqueness of the solution is usually ensured by specifying the divergence (or gauge) of \mathbf{A} together with the necessary boundary conditions. Thus in a conductive region, the field equations in terms of \mathbf{A} and \mathcal{V} (for the magnetostatic motion-related problems are:

$$\nabla \times \frac{1}{\mu} \nabla \times \mathbf{A} + \sigma \left(\frac{\partial \mathbf{A}}{\partial t} + \nabla \mathcal{V} \right) = \mathbf{J}_s + \sigma \mathbf{V} \times \mathbf{B} \quad (7.3)$$

$$\nabla \cdot \sigma \left(\frac{\partial \mathbf{A}}{\partial t} + \nabla \mathcal{V} \right) = 0. \quad (7.4)$$

Modified Vector Potential Formulation

In the modified magnetic vector potential formulation, the following substitution is made in Equation 7.3:

$$\frac{\partial \mathbf{A}^*}{\partial t} = \frac{\partial \mathbf{A}}{\partial t} + \nabla \mathcal{V} \quad (7.5)$$

This results in the governing equation:

$$\nabla \times \frac{1}{\mu} \nabla \times \mathbf{A}^* = \mathbf{J}_S - \sigma \frac{\partial \mathbf{A}^*}{\partial t} + \sigma \mathbf{V} \times \nabla \times \mathbf{A}^* \quad (7.6)$$

If $\nabla \mathcal{V}$ is chosen to be zero, the formulation is same as the MVP formulation used in the axisymmetric formulations. This formulation requires that the unknown variable \mathbf{A} be continuous in the entire solution region. In two dimensional and axisymmetric cases, \mathbf{A} has only one component and is continuous in the direction perpendicular to the plane of solution. Hence discontinuities in motionally induced currents across conductor boundaries will not result in a discontinuity of \mathbf{A} . In the 3D case, \mathbf{A} has all three components and is discontinuous across conductor boundaries. Hence, this formulation is inaccurate if nodal elements are used to model 3D geometries. There are other problems associated with using nodal elements in solving 3D magnetostatic problems and these are discussed in the following section.

Nodal Element Formulations

Classical FEM methods use nodal elements, where the unknown variable is calculated at the nodes. The shape functions used in this case are scalars and hence these elements are ideally suited to the calculation of scalar quantities. The finite element approximation using nodal elements is expressed as:

$$\psi = \sum_k \psi_k N_k \quad (7.7)$$

where the subscript k stands for the node number and N_k is the scalar shape function corresponding to that node.

Nodal elements are also employed to compute vectors by considering the vector as a triplet of scalars, and the approximation is:

$$\mathbf{A} = \sum_k \mathbf{A}_k N_k \quad (7.8)$$

This method of computing vector quantities, using scalar elements, has proven to be extremely useful in 2D modeling. However, in 3D modeling, this method encounters several problems including: (a) difficulty in ensuring the divergence condition, (b) difficulty of imposing material interface conditions, and (c) field singularities at conductor corners.

Divergence condition

The governing equation for magnetostatic, motion-related problems (MVP formulation) is:

$$\nabla \times \frac{1}{\mu} \nabla \times \mathbf{A} = \mathbf{J}_s - \sigma \frac{\partial \mathbf{A}}{\partial t} + \sigma \mathbf{V} \times \nabla \times \mathbf{A} \quad (7.9)$$

This, however, does not determine \mathbf{A} uniquely, because if \mathbf{A} is a solution to Equation 7.6, any function that can be written as $\mathbf{A}' = \mathbf{A} + \nabla f$ is also a solution regardless of the form of f . Thus to determine \mathbf{A} uniquely, one must impose a condition on its divergence (Helmholtz's theorem tells us that any general vector field is determined to within an additive constant if both its divergence and its curl are specified everywhere). Such a condition is called a gauge condition, and one choice is the Coulombs gauge:

$$\nabla \cdot \mathbf{A} = 0 \quad (7.10)$$

This condition of Coulombs gauge is naturally satisfied in the 2D and axisymmetric cases since there is only one component of \mathbf{A} , which is perpendicular to the plane of interest and constant along that direction. In 3D formulations Coulombs gauge has to be enforced. However, if the goal is to compute the magnetic flux density \mathbf{B} , Equation 7.6 yields valid results without enforcing Coulombs gauge. Or, in other words, the nonuniqueness of \mathbf{A} does not affect the uniqueness of the magnetic flux density computation [30]. This is true of general magnetostatic problems, and formulations have been used without Coulombs gauge yielding accurate results [53] - [58]. Numerical results show that indeed the solution to \mathbf{A} is not divergenceless, but the solution to \mathbf{B} is always unique. However, since no attempt was made to enforce the gauge condition in the formulation, there is some controversy regarding the validity of such methods [59] - [63].

Interface conditions

As seen before, in the finite element analysis it is essential to apply boundary conditions to render a unique solution. When the problem involves conductive edges and corners, it is essential to specify the fields at edges and corners. However, this cannot be easily done with the basis functions obtained by interpolating the nodal fields. Consider the example shown in Figure 7.1. Here, suppose that currents (which are proportional to \mathbf{A}) have to be specified on the edges (AB and BC) of the conductive material. The directions of the current are indicated in the figure. Since in nodal element formulations the values are specified at the nodes, node B must be specified with the appropriate values of \mathbf{A} , to represent the conditions in Figure 7.1. As can be seen, this is not possible (with the \mathbf{A} formulation) while still maintaining zero currents in the non-conductive region.

Corner singularities

The problem of corner singularity follows from the problem of enforcing interface conditions. \mathbf{A} is proportional to the induced current density which takes a local maximum at concave corner points. Hence the value of \mathbf{A} at these points in the geometry should have a finite non-zero value. However, the interface condition of

$$\mathbf{A} \cdot \hat{\mathbf{n}} = 0 \quad (7.11)$$

which should be enforced on the conductor-nonconductor interface leads to a zero value of \mathbf{A} at the corner.

The problem with interface conditions and the resulting corner singularities may be over come by using the $\mathbf{A} - V$ formulation. However, this introduces an additional

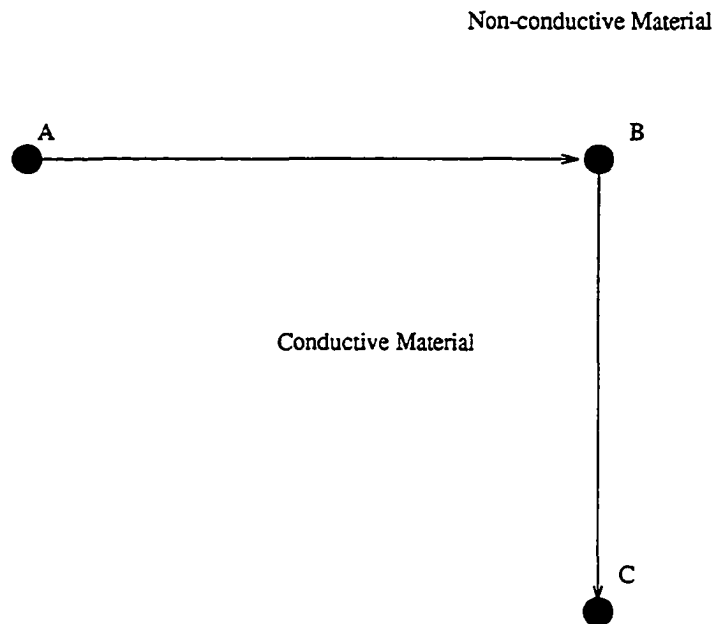


Figure 7.1: Difficulty of imposing interface conditions with nodal elements

scalar electric potential into the formulation. Another approach used to solve this problem is to round off the corners artificially. This approach seems very simple, but it is associated with two problems. The first concerns the modeling error introduced by the rounding off of the corners. It is true that rounding off the corners would result only in local errors and therefore the errors introduced should be negligible. However, there has been no attempt to quantify the errors, and hence the approach cannot be validated. The second problem concerns the finite element mesh. To model accurately a rounded corner with a large curvature, it is necessary to use very small elements, which not only increases the number of unknowns dramatically but also make the task of mesh generation very difficult.

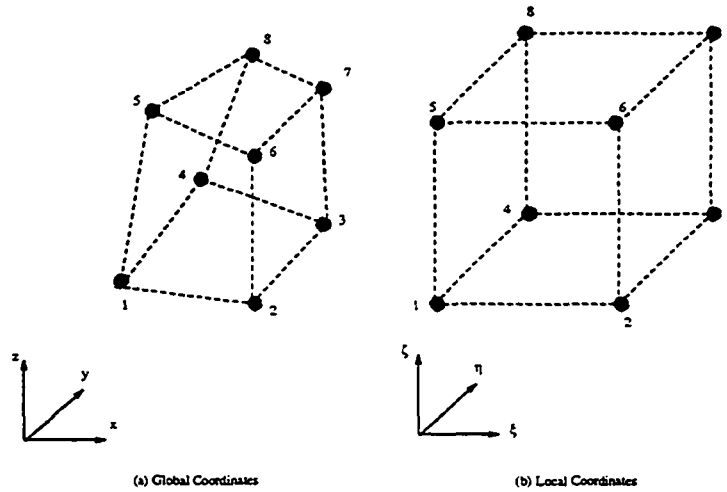


Figure 7.2: Hexahedral nodal element

Constructing nodal elements

The shape functions for the eight node hexahedral element (Figure 7.2) are derived from the *serendipity family* of elements [39], [64]. Here, each shape function N_k is required to have a value of 1 at node k and zero at every other node of the element. The shape function for the k -th node can be written as (for local coordinates varying from 0 - 1):

$$N_k = C (1 - \xi_k \xi) (1 - \eta_k \eta) (1 - \zeta_k \zeta) \quad (7.12)$$

For the particular choice of coordinates shown in Figure 7.2, constant $C = 1$. The shape functions for the eight nodes are tabulated in Table 7.1.

Table 7.1: Shape functions for nodal elements

<i>Node Number</i>	<i>Shape Function</i>
1	$(1 - \xi)(1 - \eta)(1 - \zeta)$
2	$\xi(1 - \eta)(1 - \zeta)$
3	$\xi\eta(1 - \zeta)$
4	$(1 - \xi)\eta(1 - \zeta)$
5	$(1 - \xi)(1 - \eta)\zeta$
6	$\xi(1 - \eta)\zeta$
7	$\xi\eta\zeta$
8	$(1 - \xi)\eta\zeta$

Edge Element Formulations

Recently, edge elements, where the shape functions are vectors, have been shown to be better suited for modeling vector fields in three dimensions. The edge-based FEM method has been shown to be free of all the previously mentioned shortcomings associated with nodal elements. The finite element approximation using edge elements is:

$$\mathbf{A} = \sum_m A_m \mathbf{N}_m \quad (7.13)$$

Here, the subscript m is the edge number, \mathbf{N}_m is the vector shape function corresponding to that edge and A_m is the projection of \mathbf{A} on to the edge m .

Construction of edge elements

There are several choices of shape functions available, in general they have the form (for local coordinates varying from 0 - 1):

$$\mathbf{N}_m = C(1 - \xi_m \xi)(1 - \eta_m \eta) \nabla \zeta \quad (7.14)$$

for edges in the ζ direction.

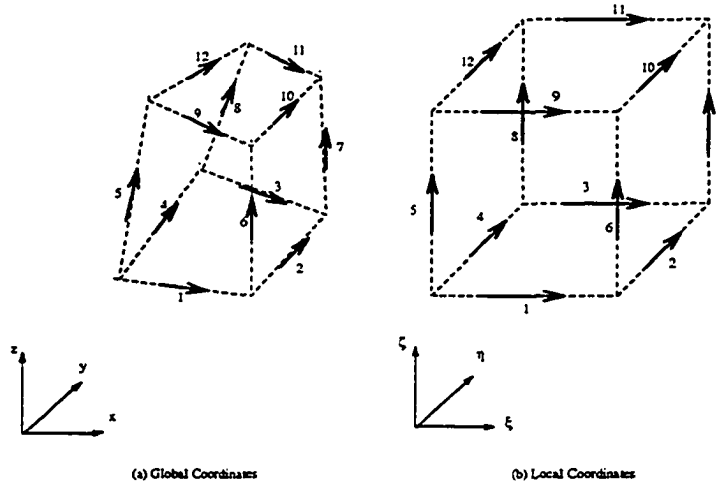


Figure 7.3: Hexahedral edge element

$$\mathbf{N}_m = C(1 - \xi_m \xi)(1 - \zeta_m \zeta) \nabla \eta \quad (7.15)$$

for edges in the η direction, and

$$\mathbf{N}_m = C(1 - \eta_m \eta)(1 - \zeta_m \zeta) \nabla \xi \quad (7.16)$$

for edges in the ξ direction.

The shape functions used in this work, corresponding to the hexahedral element shown in Figure 7.3, are tabulated in Table 7.2.

Properties of edge elements

An important feature of these shape functions is that \mathbf{N}_m has a tangential component only along the m -th edge and none along all the other edges. Thus, the continuity of the tangential field across all elements is guaranteed. Simultaneously,

Table 7.2: Shape functions for edge elements

<i>Edge Number</i>	<i>Shape Function</i>
1	$(1 - \eta - \zeta + \eta\zeta) \xi$
2	$(\xi - \xi\zeta) \eta$
3	$(\eta - \eta\zeta) \xi$
4	$(1 - \zeta - \xi + \xi\zeta) \eta$
5	$(1 - \xi - \eta + \xi\eta) \zeta$
6	$(\xi - \xi\eta) \zeta$
7	$(\xi\eta) \zeta$
8	$(\eta - \xi\eta) \zeta$
9	$(\zeta - \eta\zeta) \xi$
10	$(\xi\zeta) \eta$
11	$(\eta\zeta) \xi$
12	$(\zeta - \xi\zeta) \eta$

edge elements allow for the discontinuity of the normal field. Hence, edge elements can be used in formulations with \mathbf{E} , \mathbf{H} , \mathbf{B} , \mathbf{D} , \mathbf{J} or \mathbf{A} , all of which are discontinuous at interfaces. Another unique feature of these functions is that each satisfies the divergence condition $\nabla \cdot \mathbf{N}_m = 0$ within the region of the element (using brick elements). Therefore, they are ideal for representing vector fields. Also, referring back to the problem of specifying interface conditions (Figure 7.1), since \mathbf{A} is now specified on the edges of the element, it is easy to specify \mathbf{A} along the edges to represent the conditions in Figure 7.1, without introducing currents in the nonconductive regions.

Edge Element Based Mesh Generation

The mesh generator for the edge element formulation involves generating the connectivity matrix for each element in terms of global edge numbers. Hence, the mesh has to be visualized and constructed in terms of edges rather than with the

familiar nodes. The first step is to compute the number of edges. Computing the total number of edges is not as intuitive as computing the total number of nodes. The total number of nodes is given by:

$$NUMNP = NUMX * NUMY * NUMZ \quad (7.17)$$

where NUMNP is the number of node points; NUMX, NUMY, NUMZ are the number of nodes in the x, y and z directions respectively. However the total number of edges is given by:

$$\begin{aligned} NUMED = & (NUMX - 1) + (NUMX * 2 - 1) * (NUMY - 1) \\ & + ((NUMX * 2 - 1) + (NUMX * 3 - 1) * (NUMY - 1)) * (NUMZ - 1) \end{aligned} \quad (7.18)$$

where NUMED is the number of edges.

The next step is to build the connectivity matrix for each element in terms of edges. The local numbering scheme is shown in Figure 7.3. The global numbering scheme used in this work is shown in Figure 7.4. This is a very important step in the mesh generation as the bandwidth of the global matrix used in the finite element solution is determined by the global numbering scheme. In this work, the numbering is done plane by plane. The minimum bandwidth can be achieved by numbering the plane containing the minimum number of edges consecutively.

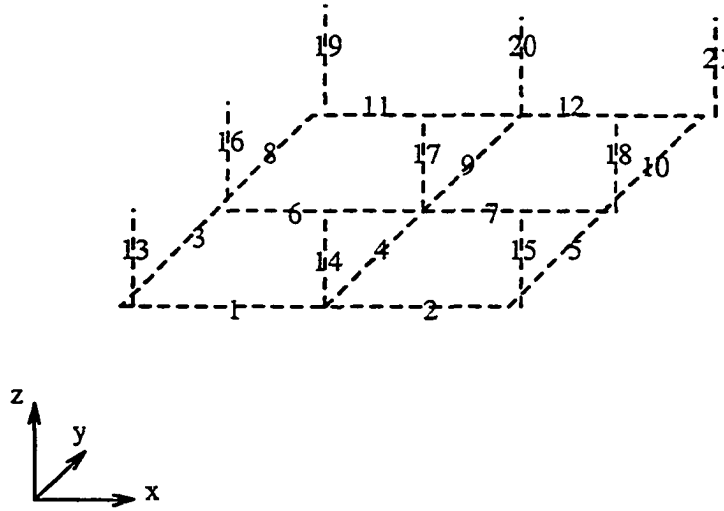


Figure 7.4: Global numbering scheme

Formulation for the 3D Magnetostatic Motion-related Problem

The governing equation of the magnetostatic, motion-related problems is presented in Equation 7.6. The curl-curl term and the velocity term are expanded separately for convenience.

The curl-curl term

The $\nabla \times \frac{1}{\mu} \nabla \times \mathbf{A}$ term is approximated as $\frac{1}{\mu} \nabla \times \nabla \times \mathbf{A}$, assuming linearity of permeability within each element. Expanding this term in 3D yields:

$$\frac{1}{\mu} \nabla \times \nabla \times \mathbf{A} = \frac{1}{\mu} \left(\frac{\partial}{\partial y} \frac{\partial A_y}{\partial x} - \frac{\partial^2 A_x}{\partial y^2} - \frac{\partial^2 A_x}{\partial z^2} + \frac{\partial}{\partial z} \frac{\partial A_z}{\partial x} \right) \hat{x}$$

$$\begin{aligned}
& + \frac{1}{\mu} \left(\frac{\partial}{\partial x} \frac{\partial A_x}{\partial y} - \frac{\partial^2 A_y}{\partial x^2} - \frac{\partial^2 A_y}{\partial z^2} + \frac{\partial}{\partial z} \frac{\partial A_z}{\partial y} \right) \hat{y} \\
& + \frac{1}{\mu} \left(\frac{\partial}{\partial x} \frac{\partial A_x}{\partial z} - \frac{\partial^2 A_z}{\partial x^2} - \frac{\partial^2 A_z}{\partial y^2} + \frac{\partial}{\partial y} \frac{\partial A_y}{\partial z} \right) \hat{z}
\end{aligned} \tag{7.19}$$

A special situation arises when brick elements are used. In Equation 7.19, consider the terms of the form:

$$\frac{\partial}{\partial y} \frac{\partial A_y}{\partial x} \tag{7.20}$$

When \mathbf{A} is expressed using Equation 7.13 and the shape functions in Table 7.2 are applied, it is apparent that the terms of the form in Equation 7.20 become zero as there is no variation of the shape function along the its own edge. Hence, Equation 7.19 can be replaced by the Laplacian:

$$\begin{aligned}
& \frac{1}{\mu} \nabla \times \nabla \times \mathbf{A} = \\
& \frac{1}{\mu} \left(-\frac{\partial^2 A_x}{\partial y^2} - \frac{\partial^2 A_x}{\partial z^2} \right) \hat{x} \\
& + \frac{1}{\mu} \left(-\frac{\partial^2 A_y}{\partial x^2} - \frac{\partial^2 A_y}{\partial z^2} \right) \hat{y} \\
& + \frac{1}{\mu} \left(-\frac{\partial^2 A_z}{\partial x^2} - \frac{\partial^2 A_z}{\partial y^2} \right) \hat{z}
\end{aligned} \tag{7.21}$$

This is an interesting topic of discussion. Previously, some researchers used the Laplacian operator while expanding the curl-curl operator in 3D with nodal elements [65]. This was met with serious opposition as it is not based on the mathematics of the problem. While with nodal elements this reduction is not possible. As demonstrated above, the use of edge elements makes possible reducing the curl-curl operator to the Laplacian. However, this is true only when brick elements are used.

The velocity term

The magnetizer being modeled in this work moves only along the axis of the pipe. Choosing the x-direction (in Cartesian coordinates) to be the direction of motion, the velocity term $\mathbf{V} \times \nabla \times \mathbf{A}$ is expressed as:

$$\mathbf{V} \times \nabla \times \mathbf{A} = -V \left(\frac{\partial A_y}{\partial x} - \frac{\partial A_x}{\partial y} \right) \hat{y} + V \left(\frac{\partial A_x}{\partial z} - \frac{\partial A_z}{\partial x} \right) \hat{z} \quad (7.22)$$

The 3D governing equation

We can now express Equation 7.6 for the 3D case being considered as (using general hexahedral elements):

$$\begin{aligned} & \frac{1}{\mu} \left(\frac{\partial}{\partial y} \frac{\partial A_y}{\partial x} - \frac{\partial^2 A_x}{\partial y^2} - \frac{\partial^2 A_x}{\partial z^2} + \frac{\partial}{\partial z} \frac{\partial A_z}{\partial x} \right) \hat{x} \\ & + \frac{1}{\mu} \left(\frac{\partial}{\partial x} \frac{\partial A_x}{\partial y} - \frac{\partial^2 A_y}{\partial x^2} - \frac{\partial^2 A_y}{\partial z^2} + \frac{\partial}{\partial z} \frac{\partial A_z}{\partial y} \right) \hat{y} \\ & + \frac{1}{\mu} \left(\frac{\partial}{\partial x} \frac{\partial A_x}{\partial z} - \frac{\partial^2 A_z}{\partial x^2} - \frac{\partial^2 A_z}{\partial y^2} + \frac{\partial}{\partial y} \frac{\partial A_y}{\partial z} \right) \hat{z} \\ = & -\mathbf{J}_s + \sigma \frac{\partial \mathbf{A}}{\partial t} - V \left(\frac{\partial A_y}{\partial x} + \frac{\partial A_x}{\partial y} \right) \hat{y} - V \left(\frac{\partial A_x}{\partial z} - \frac{\partial A_z}{\partial x} \right) \hat{z} \end{aligned} \quad (7.23)$$

This is the governing equation used to cast the problem into the finite element formulation described in the next section.

3D Galerkin finite element formulation

We now apply the Galerkin weighted residual method described in Chapter 3, and the Leismann-Frind method described in Chapter 4, to equation 7.23. In the case

of edge elements, since the shape functions and the weighting functions are vectors, the resulting Galerkin formulation involves projecting the edges in the x, y, and z directions:

$$\begin{aligned}
& \sum_{i=1}^k \int_v \left(\frac{\sigma}{\delta} N_j N_i A_{ei}^{n+1} [\hat{\mathbf{e}}_j \cdot \hat{\mathbf{x}}] [\hat{\mathbf{e}}_i \cdot \hat{\mathbf{x}}] \right) dv + \int_v \left(\frac{1}{\mu} \frac{\partial N_j}{\partial z} \frac{\partial N_i}{\partial z} A_{ei}^{n+1} [\hat{\mathbf{e}}_j \cdot \hat{\mathbf{x}}] [\hat{\mathbf{e}}_i \cdot \hat{\mathbf{x}}] \right) dv \\
& + \int_v \left(\frac{1}{\mu} \frac{\partial N_j}{\partial y} \frac{\partial N_i}{\partial y} A_{ei}^{n+1} [\hat{\mathbf{e}}_j \cdot \hat{\mathbf{x}}] [\hat{\mathbf{e}}_i \cdot \hat{\mathbf{x}}] \right) dv - \int_v \left(\frac{1}{\mu} \frac{\partial N_j}{\partial y} \frac{\partial N_i}{\partial x} A_{ei}^{n+1} [\hat{\mathbf{e}}_j \cdot \hat{\mathbf{y}}] [\hat{\mathbf{e}}_i \cdot \hat{\mathbf{x}}] \right) dv \\
& \quad - \int_v \left(\frac{1}{\mu} \frac{\partial N_j}{\partial z} \frac{\partial N_i}{\partial x} A_{ei}^{n+1} [\hat{\mathbf{e}}_j \cdot \hat{\mathbf{z}}] [\hat{\mathbf{e}}_i \cdot \hat{\mathbf{x}}] \right) dv + \int_v \left(\frac{\sigma}{\delta} N_j N_i A_{ei}^{n+1} [\hat{\mathbf{e}}_j \cdot \hat{\mathbf{y}}] [\hat{\mathbf{e}}_i \cdot \hat{\mathbf{y}}] \right) dv \\
& + \int_v \left(\frac{1}{\mu} \frac{\partial N_j}{\partial x} \frac{\partial N_i}{\partial x} A_{ei}^{n+1} [\hat{\mathbf{e}}_j \cdot \hat{\mathbf{y}}] [\hat{\mathbf{e}}_i \cdot \hat{\mathbf{y}}] \right) dv + \int_v \left(\frac{1}{\mu} \frac{\partial N_j}{\partial z} \frac{\partial N_i}{\partial z} A_{ei}^{n+1} [\hat{\mathbf{e}}_j \cdot \hat{\mathbf{y}}] [\hat{\mathbf{e}}_i \cdot \hat{\mathbf{y}}] \right) dv \\
& \quad - \int_v \left(\frac{\partial N_j}{\partial x} \frac{\partial N_i}{\partial y} A_{ei}^{n+1} [\hat{\mathbf{e}}_j \cdot \hat{\mathbf{x}}] [\hat{\mathbf{e}}_i \cdot \hat{\mathbf{y}}] \right) dv - \int_v \left(\frac{\partial N_j}{\partial z} \frac{\partial N_i}{\partial y} A_{ei}^{n+1} [\hat{\mathbf{e}}_j \cdot \hat{\mathbf{z}}] [\hat{\mathbf{e}}_i \cdot \hat{\mathbf{y}}] \right) dv \\
& + \int_v \left(\frac{1}{2} \frac{\sigma V^2 \delta}{2} \frac{\partial N_j}{\partial x} \frac{\partial N_i}{\partial x} A_{ei}^{n+1} [\hat{\mathbf{e}}_j \cdot \hat{\mathbf{y}}] [\hat{\mathbf{e}}_i \cdot \hat{\mathbf{y}}] \right) dv + \int_v \left(\frac{\sigma}{\delta} N_j N_i A_{ei}^{n+1} [\hat{\mathbf{e}}_j \cdot \hat{\mathbf{z}}] [\hat{\mathbf{e}}_i \cdot \hat{\mathbf{z}}] \right) dv \\
& + \int_v \left(\frac{1}{\mu} \frac{\partial N_j}{\partial y} \frac{\partial N_i}{\partial y} A_{ei}^{n+1} [\hat{\mathbf{e}}_j \cdot \hat{\mathbf{z}}] [\hat{\mathbf{e}}_i \cdot \hat{\mathbf{z}}] \right) dv + \int_v \left(\frac{1}{\mu} \frac{\partial N_j}{\partial x} \frac{\partial N_i}{\partial x} A_{ei}^{n+1} [\hat{\mathbf{e}}_j \cdot \hat{\mathbf{z}}] [\hat{\mathbf{e}}_i \cdot \hat{\mathbf{z}}] \right) dv \\
& \quad - \int_v \left(\frac{\partial N_j}{\partial x} \frac{\partial N_i}{\partial z} A_{ei}^{n+1} [\hat{\mathbf{e}}_j \cdot \hat{\mathbf{x}}] [\hat{\mathbf{e}}_i \cdot \hat{\mathbf{z}}] \right) dv - \int_v \left(\frac{\partial N_j}{\partial y} \frac{\partial N_i}{\partial z} A_{ei}^{n+1} [\hat{\mathbf{e}}_j \cdot \hat{\mathbf{y}}] [\hat{\mathbf{e}}_i \cdot \hat{\mathbf{z}}] \right) dv \\
& \quad + \int_v \left(\frac{1}{2} \frac{\sigma V^2 \delta}{2} \frac{\partial N_j}{\partial x} \frac{\partial N_i}{\partial x} A_{ei}^{n+1} [\hat{\mathbf{e}}_j \cdot \hat{\mathbf{z}}] [\hat{\mathbf{e}}_i \cdot \hat{\mathbf{z}}] \right) dv \\
& = \sum_{i=1}^k \int_v (N_j J_x [\hat{\mathbf{e}}_j \cdot \hat{\mathbf{x}}]) dv + \int_v \left(\frac{\sigma}{\delta} N_j N_i A_{ei}^n [\hat{\mathbf{e}}_j \cdot \hat{\mathbf{x}}] [\hat{\mathbf{e}}_i \cdot \hat{\mathbf{x}}] \right) dv + \int_v (N_j J_y [\hat{\mathbf{e}}_j \cdot \hat{\mathbf{y}}]) dv \\
& \quad - \int_v \left(\frac{1}{2} \frac{\sigma V^2 \delta}{2} \frac{\partial N_j}{\partial x} \frac{\partial N_i}{\partial x} A_{ei}^n [\hat{\mathbf{e}}_j \cdot \hat{\mathbf{y}}] [\hat{\mathbf{e}}_i \cdot \hat{\mathbf{y}}] \right) dv - \int_v \left(\sigma V N_j \frac{\partial N_i}{\partial x} A_{ei}^n [\hat{\mathbf{e}}_j \cdot \hat{\mathbf{y}}] [\hat{\mathbf{e}}_i \cdot \hat{\mathbf{y}}] \right) dv \\
& \quad + \int_v \left(\frac{\sigma}{\delta} N_j N_i A_{ei}^n [\hat{\mathbf{e}}_j \cdot \hat{\mathbf{y}}] [\hat{\mathbf{e}}_i \cdot \hat{\mathbf{y}}] \right) dv + \int_v \left(\frac{1}{\mu} \frac{\partial N_j}{\partial x} \frac{\partial N_i}{\partial x} A_{ei}^n [\hat{\mathbf{e}}_j \cdot \hat{\mathbf{z}}] [\hat{\mathbf{e}}_i \cdot \hat{\mathbf{z}}] \right) dv \\
& \quad + \int_v \left(\sigma V N_j \frac{\partial N_i}{\partial x} A_{ei}^n [\hat{\mathbf{e}}_j \cdot \hat{\mathbf{y}}] [\hat{\mathbf{e}}_i \cdot \hat{\mathbf{x}}] \right) dv + \int_v (N_j J_z [\hat{\mathbf{e}}_j \cdot \hat{\mathbf{z}}]) dv
\end{aligned}$$

$$\begin{aligned}
& - \int_v \left(\frac{1}{2} \frac{\sigma V^2 \delta}{2} \frac{\partial N_j}{\partial x} \frac{\partial N_i}{\partial x} A_{ei}^n [\hat{\mathbf{e}}_j \cdot \hat{\mathbf{z}}] [\hat{\mathbf{e}}_i \cdot \hat{\mathbf{z}}] \right) dv - \int_v \left(\sigma V N_j \frac{\partial N_i}{\partial x} A_{ei}^n [\hat{\mathbf{e}}_j \cdot \hat{\mathbf{z}}] [\hat{\mathbf{e}}_i \cdot \hat{\mathbf{z}}] \right) dv \\
& \quad + \int_v \left(\sigma V N_j \frac{\partial N_i}{\partial x} A_{ei}^n [\hat{\mathbf{e}}_j \cdot \hat{\mathbf{z}}] [\hat{\mathbf{e}}_i \cdot \hat{\mathbf{x}}] \right) dv
\end{aligned} \tag{7.24}$$

where $\hat{\mathbf{e}}_i$ and $\hat{\mathbf{e}}_j$ are unit vectors along the edges i and j respectively. The procedure is carried out for all nodes until j is the maximum number of nodes.

Jacobi transformation

The so called distorted brick element or the hexahedral element in the xyz coordinate system can be transformed into a cubic element in the new $\xi\eta\zeta$ coordinate system (Figure 7.3). The required transformation is

$$\begin{aligned}
x &= \sum_{i=1}^8 N_i^e(\xi\eta\zeta) x_i^e \\
y &= \sum_{i=1}^8 N_i^e(\xi\eta\zeta) y_i^e \\
z &= \sum_{i=1}^8 N_i^e(\xi\eta\zeta) z_i^e
\end{aligned} \tag{7.25}$$

where $N_i^e(\xi\eta\zeta)$ is the nodal shape function given by Equation 7.12 with (ξ_i, η_i, ζ_i) denoting the coordinates of the i -th node. With the intent of performing the integration in the $(\xi\eta\zeta)$ coordinate system, we first need to convert all integrands in terms of ξ , η , and ζ . The Jacobian $[J]$ is used for this transformation and it is given by:

$$\begin{bmatrix} \frac{\partial x}{\partial \xi} & \frac{\partial y}{\partial \xi} & \frac{\partial z}{\partial \xi} \\ \frac{\partial x}{\partial \eta} & \frac{\partial y}{\partial \eta} & \frac{\partial z}{\partial \eta} \\ \frac{\partial x}{\partial \zeta} & \frac{\partial y}{\partial \zeta} & \frac{\partial z}{\partial \zeta} \end{bmatrix} \quad (7.26)$$

Equation 7.26 can be expressed entirely in terms of ξ , η , and ζ in view of Equation 7.25. It can be shown that elemental volume in the xyz system can be transformed into the $\xi\eta\zeta$ system as

$$dV = dx dy dz = \det [J] d\xi d\eta d\zeta \quad (7.27)$$

Computational Aspects of 3D Edge Element Modeling

Memory considerations

Discretization using the edge element technique in 3D results in a higher number of unknowns compared to the nodal element technique (about three times with hexahedral elements). However, the higher number of unknowns is balanced by lower connectivity between edges or a greater sparsity of the finite element matrix. As a result, the memory demand for both types of elements is about the the same if only nonzero entries are counted. This comparison is valid if the unknowns are scalar quantities, in which case there is one unknown per edge with edge elements and one unknown per node with nodal elements. However, while computing vector quantities, there is still one unknown per edge with edge elements, but there are three unknowns per node with nodal elements, hence bringing down the total number of variables by a factor of three with edge elements. The matrix solver used in this work does not currently take advantage of the sparsity of the finite element matrix and is a topic of

future work discussed in Chapter 9. A general banded matrix solver is currently used in edge element code developed, for which the memory requirement is approximately the same as that of the nodal element technique.

Speed considerations

In this work DEC-ALPHA workstations have been used for running the numerical models. The DEC-ALPHA platform is a state-of-the-art workstation with the high-speed ALPHA chip providing speedups of about 15 times over conventional workstations. Also, the solver used in this work has been optimized for best performance on the DEC-ALPHA platform. The optimization is achieved by partitioning the matrix into blocks to perform the computation by matrix-matrix operations on the blocks. By organizing computation in this fashion, one can provide for full reuse of data while a given block is held in the cache or local memory. This approach avoids excessive movement of data to and from memory. The optimization technique summarized above has been described in full detail in reference [66]. These block operations are optimized for each architecture, and the general version of the corresponding routines are available in the LAPACK library developed by J.J. Dongarra et al, Computer Science Department, University of Tennessee. LAPACK is a set of linear algebra subroutines intended to supersede LINPACK, EISPACK, etc. The optimization for the DEC-ALPHA machines has been implemented by Jim Coyle, Systems Analyst, Iowa State University Computation Center. For the application described in this chapter, a speedup by a factor of six is obtained using the optimized routine in comparison to a standard Gaussian elimination routine. Another advantage of using LAPACK routines is that they are designed to perform well on

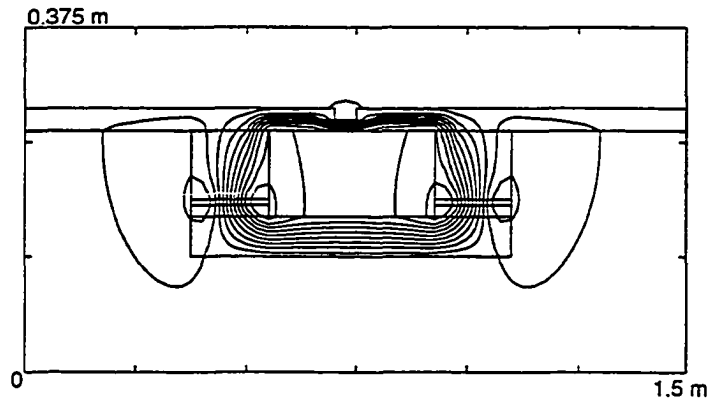


Figure 7.5: Geometry and field lines corresponding to the MVP formulation (static case)

supercomputers. Hence, the application developed can be ported on to a supercomputer without any further modifications for optimization.

Results

Preliminary validation of the edge element code is performed using a simplified 2D geometry and comparing with results from a 2D nodal element MVP formulation. The geometry and the flux lines (obtained using the edge element code) are shown in Figure 7.5. The validation is shown in Figure 7.6 for a scan line, immediately above the pipe-wall.

Also, the edge element code has been used to model velocity effects for the 2D geometry. The results are shown in Figure 7.7. The results predict the theoretically expected dragging of the flux lines as the magnetizer moves (from top to bottom).

The edge element code has also been used simulate the full 3D geometry. Results from the 3D edge element code are compared to the experimental and 3D nodal MSP

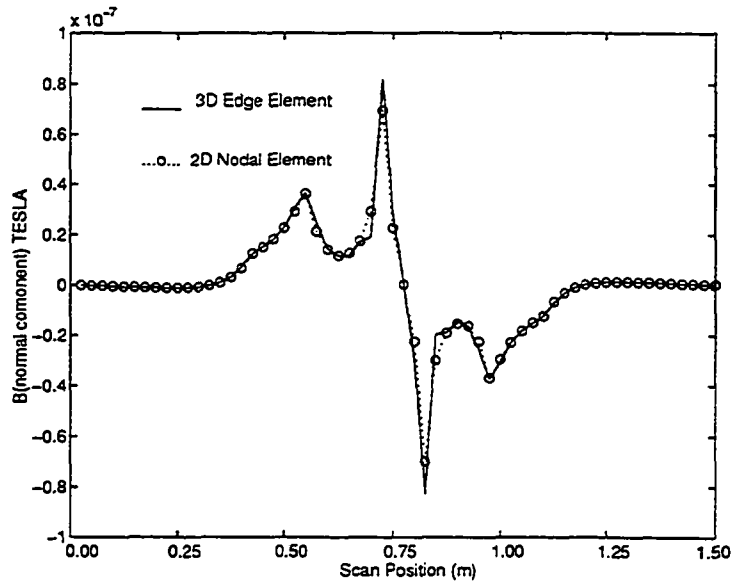


Figure 7.6: Validation of the edge element code for the 2D static case

formulation results, described in Chapter 5, for further validation. Figure 7.8 shows a comparison of B_z (predicted by the edge element MVP formulation and the nodal element MSP formulation) for a scan line directly above the pig with pig placed in air. Figure 7.9 shows the corresponding comparison between experimental results and the edge element formulation.

The results presented show an excellent comparison of the edge element code with previously validated finite element formulations and also with experiment. The good match with experiment, despite ignoring permeability effects, is because the experiment considered is with the pig in air, where the pipe-wall nonlinearities do not come into the picture. However, for accurate predictions of MFL signals, nonlinearity has to be incorporated and is discussed as part of future work in Chapter 9.

The MFL signals for the static case and the for the magnetizer moving at 5

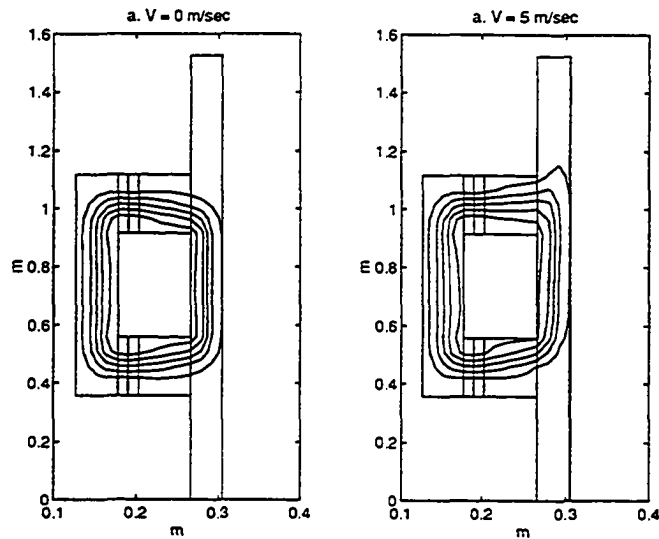


Figure 7.7: The effect of velocity on the flux lines

m/sec are presented in Figure 7.10. The defect used is 0.15 m long 0.15 m wide and 50 % deep. Also, the defect is aligned such that the magnets pass directly under it. Comparing these results with the results predicted by the linear axisymmetric code (Figure 4.2), it is seen that the predictions are similar in terms of the extent of velocity effects. Part of the future directions discussed in Chapter 9 includes the use of the 3D edge element code to study the 3D nature of velocity effects. This involves studying the effects of relative positions of defect and magnetizer on velocity effects.

Concluding, this chapter presents a new 3D formulation based on edge elements, using the Leismann-Frind method, capable of modeling velocity effects using transient analysis. Validity of the code has been demonstrated by comparing results with the nodal MVP formulation, the nodal MSP formulation and experimental results. The MFL signals predicted for the static case and with velocity are presented. The code developed is a potential tool for generating a data base of defect signals for

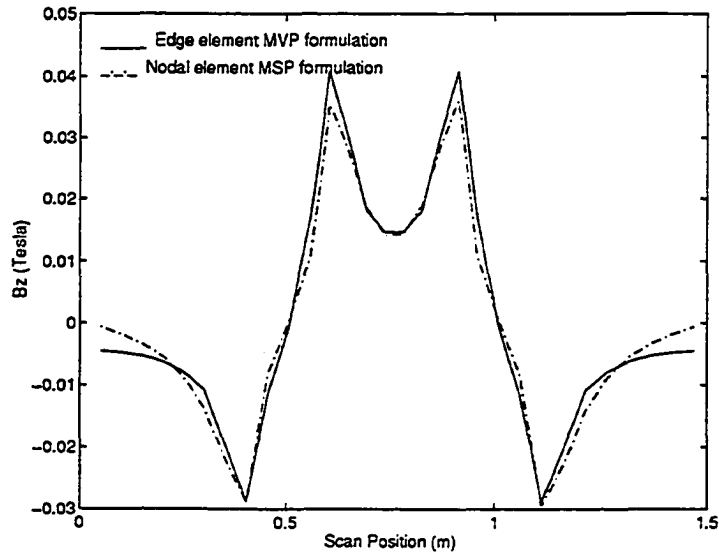


Figure 7.8: Comparison of edge element MVP formulation and nodal element MSP formulation

different velocities - for use in defect characterization; and also for an analysis of the magnetizer, for optimizing the performance of the pig for better defect characterization. Also, this is the first model capable of 3D transient analysis of velocity effects and finds use in modeling any application having nonuniform geometries and moving electromagnetic parts.

Different issues related to numerical modeling of electromagnetic phenomena have been discussed in the previous chapters including : velocity effects and permeability effects, axisymmetric and 3D methods of finite element modeling. Another important, but often ignored, aspect of numerical modeling is the data storage format for the simulation data. The next chapter discusses the importance of data storage formats and describes an implementation of a data storage format for electromagnetic modeling results.

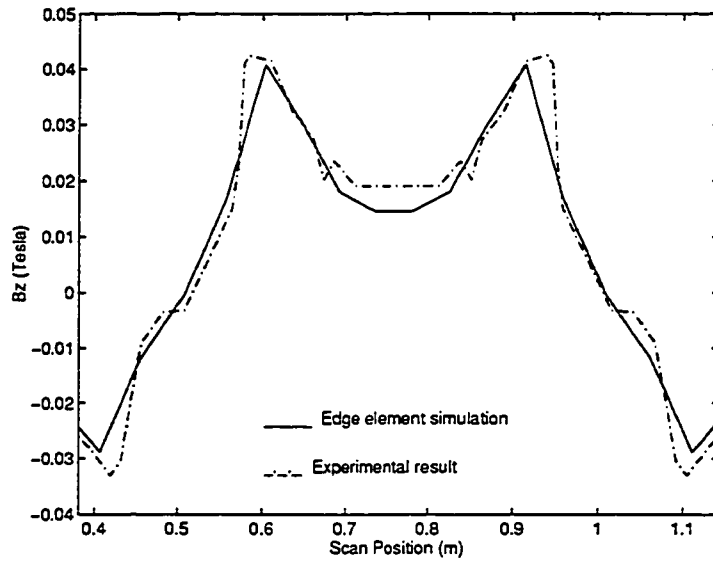


Figure 7.9: Comparison of edge element MVP formulation and experiment

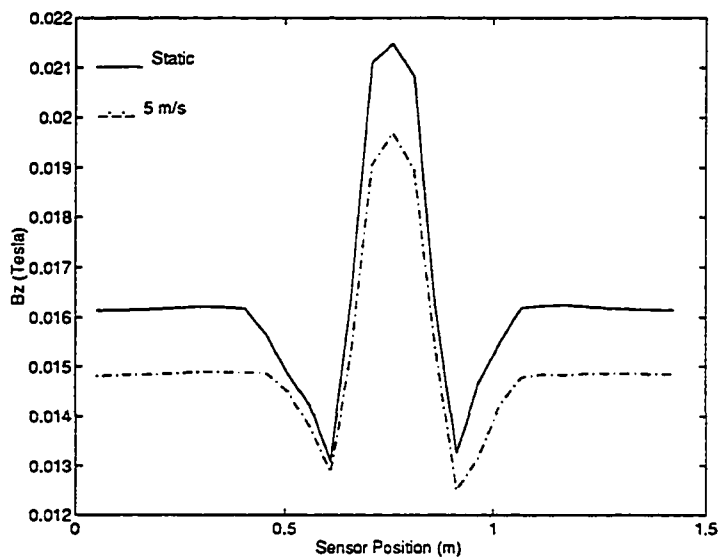


Figure 7.10: Variation of an MFL signal with velocity - a 3D prediction

CHAPTER 8. DATA-ACCESS METHODS FOR FINITE ELEMENT DATA

Introduction

Numerical modeling is a data-intensive activity. This is particularly true for the work discussed in this dissertation, where data is generated and stored for different time-steps, for different velocities, different defect dimensions, etc. The data being stored include, the different components of the magnetic flux density \mathbf{B} and the magnetic vector potential \mathbf{A} . Modern methods of producing, analyzing and visualizing data, places significant demands on the model output format. Several issues need to be considered while determining the ideal output storage format for any specific application: 1) Rapid advances in Internet technology have resulted in using a mix and match of computer platforms, for different steps in an application, to best use each platform's special features. 2) Increasing co-operation in industry has led to situations where different research groups handle different aspects of the same project. 3) Numerical modeling is a repetitive process and simulations are run for small changes in input parameters. This results in a number of files that may be similar, yet have meaningful differences. 4) Often, the data stored is not accessed as a whole. Most often only part of the data is accessed for visualization/analysis. These factors require that the data storage format be machine-independent, self describing and

direct-access.

Most existing database management systems (DBMSs) have poor support for multidimensional objects as the basic unit of data access. General-purpose database systems also perform poorly on large numerical data sets and provide, at significant costs in terms of both resources and access performance, many facilities that are not needed in the analysis, management and display of finite element data. In this dissertation netCDF, a public domain software has been evaluated to store the finite element data in an eXternal Data Representation (XDR) format. netCDF is a file format which is machine-independent, direct-access and self describing and this addresses the constraints on the model output organization described above. Several organizations, especially those involved in atmospheric sciences have adopted netCDF as a data access standard. Not much work has been recorded on the problem of storing and retrieving finite element electromagnetic simulation data. This chapter describes the application of the netCDF format for storage and retrieval of electromagnetic data.

Data Description

In the 2D axisymmetric model of the MFL inspection of pipelines, a 3D \mathbf{A} array (one dimension in time and two dimensions in space) and two dimensional B_r and B_z arrays (one dimension in time and one in space) are stored. This represents the single component of \mathbf{A} in two dimensional space for different time step positions, and \mathbf{B} values for the 1D scan line just under the pipe-wall for different time step positions. The 3D code on the other hand requires, for an equivalent case, the storage of a seven dimensional \mathbf{A} array (one dimension in time, three in space and another three

in vector space), and 3D B_r and B_z arrays (one dimension in time and two dimensions in space). Here the representation is of the three vector components of \mathbf{A} in 3D space for different time step positions, and \mathbf{B} values for a 2D scan plane directly under the pipe-wall for different time step positions. this work restricts itself to the evaluation of the netCDF format for the 2D axisymmetric case, the extension to the 3D case being straight forward.

Implementation Details

Components of a netCDF file

A netCDF file has dimensions, variables and attributes. These components can be used together to capture the meaning of data and relations among data fields in a scientific data set. The listing below shows the concepts of netCDF dimensions, variables, and attributes applied to the electromagnetic data generated by the axisymmetric code. The notation used is called CDL (network Common Data form Language). It provides an easily comprehensible text version of the structure and contents of a binary netCDF file (Figure 8.1).

The CDL notation for a netCDF file can be generated automatically by using *ncdump*, a netCDF utility program. Another netCDF utility, *ncgen*, generates a netCDF file from CDL input. The components of the netCDF file listed in Figure 8.1 are discussed in the following paragraph.

A netCDF dimension is a named integer used to specify the shape of one or more of the multi-dimensional variables contained in a netCDF file. In the example above, *t_step* is the dimension indicating the time step as the magnetizer motion is simulated; *sens_pos* is the dimension used to indicate where along the axis the sensor is

```
netcdf magdat{

dimensions:
  t_step=81,sens_pos=81,xpos=31,ypos=81;

variables:
  float BR(t_step,sens_pos);
  BR:long_name = "Radial_B_Component";
  BR:units = "Gauss";
  float BZ(t_step,sens_pos);
  BZ:long_name = "Axial_B_Component";
  BZ:units = "Gauss";
  float A(t_step,xpos,ypos);
  A:long_name = "Magnetic_Vector_Potential";
  A:units = "Webers_Per_Meter";

:velocity = "0 m/sec";

data:
  BR =
-0.163410E+01, -0.193009E+01, -0.227765E+01, .....;

  BZ =
-0.163581E+01, -0.193985E+01, -0.230120E+01, .....;

  A =
0.771413E-05, 0.911200E-05, 0.107574E-04, .....;
}
```

Figure 8.1: An example of a CDL file

placed; *xpos* and *ypos* indicate the window for which the magnetic vector potential is recorded at each time step. It should be pointed out that data for sensors distributed along the entire axis of the magnetizer have been stored, to enable a study of the additional modalities associated with the MFL magnetizer (described in Chapter 5). A NetCDF variable represents a multidimensional array of values of the same type. Here, the three variables are the radial component of the magnetic flux density, the axial component of the magnetic flux density and the magnetic vector potential. All of the variables here are of the type *float*. A netCDF attribute is meant to contain information about a netCDF variable or about an entire netCDF file. Here, the attributes contain the long names of each variable, the units of each variable, and also the velocity of the magnetizer corresponding to the entire netCDF file.

Creating and reading a netCDF file

A netCDF file can be created in two ways, the first method is using the netCDF library and the second method is to first create a CDL file and use the utility *ncgen* to create the netCDF file. In this work the second method has been adopted. The output of the FEM code is in the CDL notation described in the previous subsection, and the netCDF file is generated from this file.

The netCDF file is read using the netCDF library. A generic software can be written making no assumptions about the dimensions and variable names. All the dimensions, variables, and attributes in a netCDF file are determined by calling inquire functions. The code listing (APPENDIX B3) illustrates how information (radial component of the flux density) from a single sensor on the magnetizer is extracted for a specific length of the pipe.

Conclusions

The netCDF data format has been implemented and tested for storing electromagnetic data generated from 2D FEM of gas pipeline inspections. The format is extremely convenient to store and retrieve such data because of the following features:

Self-describing A netCDF file includes information about the data it contains.

Network-transparent A netCDF file is represented in a form that can be accessed by computers with different ways of storing integers, characters, and floating point numbers.

Direct-access A small subset of a large dataset may be accessed efficiently, without first reading through all the preceding data.

For the data described in this chapter, about 3.25 M-bytes of memory was required to store the data in regular ASCII format. With the netCDF format about 0.85 M-bytes was required. On compressing the ASCII file the memory required was 0.8 M-bytes, and on compressing the netCDF file the memory required was about 0.30 M-bytes. Hence netCDF, though not intended for data compression, provides certain advantage in terms of memory requirements.

CHAPTER 9. CONCLUSIONS

The contributions of this work can be grouped into two categories. The first category being application of existing techniques to the analysis and design of the magnetizer used in the MFL inspection of gas pipelines. The second category is the implementation of a new technique, capable of modeling velocity effects using transient analysis for 3D geometries. This chapter summarizes these contributions and also dwells on the future directions for this research.

Summary of Accomplishments

Tool design

Examples of tool design ideas contributed by this work include the minimization of velocity effects, achieved by modifying the magnet configuration. This is a unique approach to the compensation of velocity effects, in that it is based on observations of how velocity affects flux lines and the compensation is built into the tool without the requirement of post processing. Another important area of contribution to tool design improvement is the investigation and demonstration of the presence of additional modalities associated with the MFL magnetizer. This provides the basis for a novel approach to data fusion, in which data from different physical phenomena are tapped from a single tool without additional hardware requirements. These ideas represent

a significant contribution to pipeline inspection methodology.

Analysis of the MFL signals

A major portion of this research is spent on analyzing the nature of velocity effects and permeability effects and their ramifications on the MFL signal. The origin of the velocity effects has been described, and the differences between upwinding methods and transient analysis methods has been quantified. The variation of permeability in the vicinity of the defect has been studied in detail, providing significant insight into the differences between axisymmetric and nonaxisymmetric magnetizers; also this study provides a quantification and an understanding of the errors introduced by an axisymmetric assumption for nonaxisymmetric geometries. Though this analysis mainly contributes to an increased understanding of the physics of pipeline inspection, it also provides a general understanding of electromagnetic behavior in the presence of moving parts.

3D edge element code capable of modeling velocity effects

The biggest contribution of this work is the development of the 3D edge element code capable of modeling velocity effects. The formulation developed using the Leismann-Frind method with 3D edge elements is an original contribution of this dissertation. The capability of modeling velocity effects in 3D using transient analysis approaches did not exist prior to this research. This capability is not only important in the area of pipeline inspection, but in many other applications involving moving electromagnetic parts with non-uniform geometries. The edge element approach is a recent technique and has many advantages in modeling vector electromagnetic fields

as described in Chapter 7. Exciting research and new developments are still underway on the use of edge elements, hence using edge elements will also enable full advantage to be taken of these developments in the future.

Future Directions

Optimizing the matrix solver

The matrix solver currently being used in the edge element finite element code is a direct Gaussian elimination type routine. This routine does not take advantage of the sparsity of the finite element matrix. For the edge element code the memory requirements are drastically reduced when only the non-zero elements of the matrix are used for the solution (refer to Chapter 7). Hence, an immediate direction for future work is to use an Incomplete-Cholesky-Conjugate-Gradient (ICCG) solver. However, with edge elements, the resulting matrices are shown to be singular, exhibiting poor and unreliable convergence if the equations are solved with the conjugate gradient method [67]. Albanese and Rubinacci have shown that one may convert the singular matrices obtained with edge-based solutions of magnetostatic problems into nonsingular matrices by setting the vector potential on the tree of the graph of the finite element mesh to zero [68]. A generalized tree-cotree gauge for magnetic field computation has been described by Manges and Cendes in [67]. The tree-cotree gauge has to be incorporated into the edge element code and the matrix solver changed to ICCG in order to take full advantage of the edge-based finite element technique.

Incorporating nonlinearity into the 3D edge element code

As described in Chapter 5, the inclusion of permeability effects into the simulation is imperative for quantitatively accurate results. Incorporating nonlinear permeability into the edge element code is straight forward and simple, however, the ICCG solver must be first incorporated into the code in order to solve the full pig geometry including velocity and permeability effects, in reasonable amounts of CPU time. The algorithm for incorporating nonlinear permeability into the axisymmetric formulation, described in Chapter 5, can be used even for the 3D formulation.

Analyzing the 3D nature of velocity effects

Another exciting area for future research is a study of the 3D nature of velocity effects. This study involves studying the influence the relative orientation of the defect and the magnetizer has on velocity effects. As, the MFL signals obtained experimentally have proven to be erratic and different for each run of the pig with the same defect set, the state-of-the-art in defect characterization is extremely poor. This study could provide answers which can greatly improve defect characterization in pipeline inspection.

BIBLIOGRAPHY

- [1] D.L. Atherton, C. Jagadish, P. Laursen, V. Storm, F. Ham and B. Scharfenberger, "Pipeline inspection tool speed alters MFL signals," *Oil and Gas Journal*, pp. 84-86, January 29, 1990.
- [2] O.J. Lodge, "On some problems connected with the flow of electricity in a plane," *Philosophy of magnetism*, 5th series, pp. 373-389, 1876.
- [3] G.F.C Searle, "On the magnetic field due to a current in a wire placed parallel to the axis of a cylinder of iron," *The Electrician*, pp. 453 and 510, 1898.
- [4] J.J. Thompson, *Recent researches in electricity and magnetism*, New York: Oxford University Press, 1893.
- [5] F.W. Carter, "A note on airgap and interpolar induction," *Journal of the Institution of Electrical Engineers*, vol. 29, pp. 925, 1900.
- [6] L.D. Kovach, *Boundary-value problems*, Reading, MA: Addison-Wesley, pp. 355-379, 1984.
- [7] G. Kron, "Numerical solution of ordinary and partial differential equations by means of equivalent circuits," *Journal of Applied Physics*, vol. 16, pp. 172-186, March 1945.

- [8] W.J.R Hofer, "The transmission-line matrix method—theory and applications," *IEEE Transactions on Microwave Theory and Techniques*, vol. MTT-33, no. 10, pp. 882-893, October 1985.
- [9] M.O. Sadiku, *Numerical techniques in electromagnetics*, Boca Raton, FL: CRC Press, 1992.
- [10] A. Thom and C.J. Apelt, *Field computations in engineering and physics*, New York: Van Nostrand, 1961.
- [11] A.A. Winslow, "Numerical solution of the quasi-linear Poisson equation in a non-uniform triangular mesh," *Journal of Computational Physics*, pp. 149, 1971.
- [12] R. Palanisamy and W. Lord, "Finite element modeling of electromagnetic NDT phenomena," *IEEE Transactions on Magnetics*, vol. MAG-15, no. 6, pp 1479-2441, November 1979.
- [13] H. Whitney, *Geometric integration theory*, Princeton, NJ: Princeton University Press, 1957.
- [14] J.C. Nedelec, "Mixed finite elements in R^3 ," *Numerical Methods*, vol. 35, pp. 315-341, 1980.
- [15] A. Bossavit and J.C. Verite, "A mixed FEM-BIEM method to solve 3-D eddy current problems," *IEEE Transactions on Magnetics*, vol. MAG-18, pp. 431-435, March 1982.

- [16] M. Hano, "Finite-element analysis of dielectric-loaded waveguides," *IEEE Transactions on Microwave Theory and Techniques*, vol. MTT-32, pp. 1275-1279, October 1984.
- [17] G. Mur and A.T. de Hoop, "A finite-element method for computing three-dimensional electromagnetic fields in inhomogeneous media," *IEEE Transactions on Magnetics*, vol. MAG-21, pp. 2188-2191, Nov. 1985.
- [18] J.S. van Welij, "Calculations of eddy current in terms of H on hexahedra," *IEEE Transactions on Magnetics*, vol. MAG-21, pp. 2239-2241, November 1985.
- [19] A. Kameari, "Three dimensional eddy current calculations using edge elements for magnetic vector potential," *Applied Electromagnetics in Materials; Pergamon press*, pp. 225-236, 1986.
- [20] M.L. Barton and Z.J. Cendes, "New vector finite elements for three-dimensional magnetic field computation," *Journal of Applied Physics*, vol. 61, no. 8, pp. 3919-3921, April 1987.
- [21] J.F. Kiefner, R.W. Wright, and R.J. Eiber, *Final report on the NDT needs for pipeline integrity assurance*, Arlington, VA: American Gas Association, 1986.
- [22] R.W.E. Shannon and L. Jackson, "Flux leakage testing applied to operational pipelines," *Materials Evaluation*, vol. 46, pp. 1516-1524, 1988.
- [23] J.C. Hamilton, "Model evaluates pipeline inspection sensors," *Oil and Gas Journal*, pp. 80-82, September 4, 1989.

- [24] W. Lord, J.M. Bridges and R. Palanisamy, "Residual and active leakage fields around defects in ferromagnetic materials," *Materials Evaluation*, pp. 47-54, July 1978.
- [25] R.W.E. Shannon and C.J. Argent, "Maintenance strategy set by cost, effectiveness," *Oil and Gas Journal*, pp. 41-44, February 6, 1989.
- [26] R.W.E. Shannon, "Intelligent pigs prove valuable," *Pipeline and Gas Journal*, pp. 14-16, October 1987.
- [27] R.W.E Shannon, "Development, operating experience prove value of British Gas' on-line inspection," *Pipeline and Gas Journal*, pp. 12-19, July 1985.
- [28] R.W.E Shannon, J.C. Braithwaite and L.L. Morgan, "Flux-leakage vehicles pass tests for pipeline inspection," *Oil and Gas Journal*, pp. 48-58, August 8, 1988.
- [29] D.D. Mackintosh, D.L. Atherton, P.C. Porte and A. Teitsma, "Test rigs for magnetic flux leakage inspection tools for pipelines," *Materials Evaluation* pp. 13-17, January 1992.
- [30] J. Jin, *The finite element method in electromagnetics*, Chichester, NY: John Wiley and Sons, 1993.
- [31] K. Muramatsu, T. Nakata, N. Takahashi and K. Fujiwara, "Comparison of coordinate systems for eddy current analysis in moving conductors," *IEEE Transaction on Magnetics*, vol. 28, pp. 1186-1189, 1992.

- [32] D. Rodger, T. Karaguler and P.J. Leonard, "A formulation for 3D moving conductor eddy Current problems," *IEEE Transactions on Magnetics*, vol. 25, pp. 4147-4149, 1989.
- [33] Y. Marechal and G. Meunier, "Computation of 2D and 3D eddy currents in moving conductors of electromagnetic retarders," *IEEE Transactions on Magnetics*, vol. 26, pp. 2382-2384, 1990.
- [34] Y. K. Shin and W. Lord, "Numerical modeling moving probe effects for electromagnetic NDE," *IEEE Transactions on Magnetics*, pp. 1865-1868, March 1993.
- [35] Y. S. Sun, W.Lord, G. Katragadda and Y.K. Shin, "Motion induced remote field eddy current effect in a magnetostatic non-destructive testing tool: a finite element prediction," *IEEE Transactions on Magnetics*, vol. 29, pp. 3304-3307, September 1994.
- [36] R.H. Hoole, "Rotor motion in dynamic finite element analysis of rotating electrical machinery," *IEEE Transactions on Magnetics*, vol. 21, pp. 2292 - 2295, 1985.
- [37] H. M. Leismann and E. O. Frind, "A symmetric - matrix time integration scheme for the efficient solution of advection - dispersion problems," *Water Resources Research*, vol. 25, pp. 1 133 - 1139, 1989.
- [38] J. Donea, "A Taylor-Galerkin method for convective transport problems," *International Journal of Numerical Methods in Engineering*, vol. 20, pp. 101 - 119, 1984.

- [39] O.C. Zienkiewicz, R. Loehner, K. Morgan and S. Nakazawa, "Finite elements in fluid mechanics - a decade of progress," *Finite Elements in Fluids*, vol. 5, pp.1-26, 1984.
- [40] Y.K. Shin, *Numerical modeling of probe velocity effects for electromagnetic NDE*, Ph.D. Dissertation, Iowa State University, 1992.
- [41] J. Traub, *Iterative methods for the solution of equations*, Englewood Cliffs, NJ: Prentice Hall, 1964.
- [42] A. Ostrowski, *Solution of equations and systems of equations*, New York: Academic Press, 1960.
- [43] W. Davidon, "Variable metric methods for minimization," *A.E.C Research and Development Report, ANL-5990, Argonne National Laboratory*, 1959.
- [44] E. Lahaye, "Solution of systems of transcendental equations," *Royal Academy of Belgium, Bulletin of Clinical Sciences*, pp. 141-146, 1948.
- [45] G. Forsythe and W. Wasow, "Finite difference methods of partial differential equations," *Wiley*, 1960.
- [46] W. Lord, "Magnetic flux leakage for measurement of crevice gap clearance and tube support plate inspection," *EPRI NP-1427, Project S125-1, Final Report*, June 1990.
- [47] W. Lord and R. Palanisamy, "Magnetic probe inspection of steam generator tubing," *Materials Evaluation*, vol. 38, pp. 38-40, 1980.

- [48] D. L. Atherton and P. Laursen, "A test rig for dynamic measurements of magnetic flux leakage patterns," *British Journal of NDT* vol. 33, pp. 69-73, 1991.
- [49] T.R. Schmidt, "History of the remote-field eddy current inspection technique," *Materials Evaluation*, vol. 47, pp. 14-22, 1989.
- [50] T.R. Schmidt, "The remote-field eddy current inspection technique," *Materials Evaluation*, vol. 42, pp. 225-230, February 1984.
- [51] W. Lord, Y.S. Sun, S.S. Udpa and S. Nath, "A finite element study of the remote field eddy current phenomenon," *IEEE Transactions on Magnetics*, vol. 24, pp. 435-438, 1988.
- [52] J.B. Nestleroth, "Remote field eddy current detection of stress corrosion cracks in gas transmission pipelines," *Review of Progress in Quantitative NDE*, vol. 10, pp. 935-942, 1991.
- [53] N. Ida, *Three dimensional finite element modeling of electromagnetic nondestructive testing phenomena*, Ph.D. Dissertation, Colorado State University, 1986.
- [54] N.A. Demerdash, T.W. Nehl, and F.A. Fouad, "Finite element formulation and analysis of three dimensional problems," *IEEE Transactions on Magnetics*, vol. MAG-16, pp. 1092-1094, 1980.
- [55] N.A. Demerdash, T.W. Nehl, F.A. Fouad, and O.A. Mohammed, "Three dimensional finite element vector potential formulation of magnetic fields in elec-

- tric apparatus," *IEEE Transactions on Power Apparatus Systems*, vol. PAS-100, pp. 4104-4111, 1981.
- [56] N.A. Demerdash, T.W. Nehl, O.A. Mohammed, and F.A. Fouad, "Experimental verification and application of the three dimensional finite element magnetic vector potential method in electric apparatus," *IEEE Transactions on Power Apparatus Systems*, vol. PAS-100, pp. 4112-4122, 1981.
- [57] F.L. Zeisler and J.R. Brauer, "Automotive alternator electromagnetic calculations using three dimensional finite elements," *IEEE Transactions on Magnetics*, vol. MAG-21, pp. 2453-2456, 1985.
- [58] S.R.H. Hoole, R. Rios, and S. Yoganathan, "Vector potential formulations and finite element trial functions," *International Journal of Numerical Methods in Engineering*, vol. 26, pp. 95-108, 1988.
- [59] M.V.K Chari, Z.J. Cendes, P.P. Silvester, A. Konard and M.A. Palmo, "Three dimensional magnetostatic field analysis of electrical machinery by the finite element method," *IEEE Transactions on Power Apparatus Systems*, vol. PAS-100, pp. 4007-4019, 1981.
- [60] P.R. Kotiuga and P.P. Silvester, "Vector potential formulation for three-dimensional magnetostatics," *Journal of Applied Physics*, vol. 53, no. 11, pp. 8399-8401, 1982.
- [61] Z.J Cendes, J. Weiss, and S.R. Hoole, "Alternative vector potential formulation of 3-D magnetostatic field problems," *IEEE Transactions on Magnetics*, vol. MAG-18, pp. 367-372, 1982.

- [62] O.A. Mohammed, W.A. Davis, B.D. Popovic, T.W. Nehl and N.A. Demerdash, "On the uniqueness of solution of magnetostatic vector potential problems by three-dimensional finite elements," *Journal of Applied Physics*, vol. 53, no. 11, pp. 8402-8404, 1982.
- [63] O.A. Mohammed, N.A. Demerdash, and T.W. Nehl, "Validity of finite element formulation and solution of three dimensional magnetostatic problem in electrical devices with application to transformers and reactors," *IEEE Transactions on Power Apparatus Systems*, vol. PAS-103, pp. 1848-1853, 1984.
- [64] J.G. Ergatodius, B.M. Irons and O.C. Zienkiewicz, "Curved isoparametric quadrilateral elements for finite element analysis," *International Journal of Solids and Structures*, vol. 4, pp. 31-42, 1968.
- [65] A. Konard, "The zero divergence constraint in 3D vector finite element methods," *The International Journal for Computation and Mathematics in Electrical and Electronic Engineering*, vol. 9, pp. 7-16, 1990.
- [66] J.J. Dongarra, P. Mayes, G.R. Brozolo, "The IBM RISC System/6000 and Linear Algebra Operations", *Univ. of Tennessee technical report CS-90-122*.
- [67] J.B. Manges and Z.J. Cendes, "A generalized tree-cotree gauge for magnetic field computation," *IEEE Transactions on Magnetics*, vol. 31, pp. 1342 - 1347, 1995.
- [68] R. Albanese and G. Rubinacci, "Magnetostatic field computations in terms of two-component vector potentials," *International Journal for Numerical Methods*, vol. 29, pp. 515-532, 1990.